Rijksuniversiteit Groningen

Msc Astronomy

Modelling the lower kHz QPO of 4U 1636−53 using a simple two-component model

Author:
Gijs de Goeijen

Supervisor:
Prof. dr. Mariano Méndez

September 2014

Abstract

Kilohertz quasi-periodic oscillations (kHz QPOs) show the fastest variability in any observed astronomical source to date. These systems usually show a pair of QPOs, called respectively, the lower and upper kHz QPOs according to their frequencies. The properties of kHz QPOs are still being extensively studied. In this thesis I try to use some basic properties of kHz QPOs, most importantly the amplitude and energy dependent time lag of the variability to try and constrain some physical properties of the system, such as the size of the corona around the neutron star in a low-mass X-ray binary. To this end I use a simple two-component model consisting of a blackbody (to represent emission from the neutron star) and a power-law component (to represent emission from a corona of hot electrons around the system) to model the lower kHz QPO of the source 4U 1636−53. Even though the model used is simple, it gives the correct trends for time lag and rms fractional amplitude as a function of energy when compared to observational data in the literature. The size of the corona found for this model is 56 km, which is comparable to previously found results for more sophisticated models.

Contents

Chapter 1

Introduction

In this section I will first give a short introduction to neutron star low-mass X-ray binaries and kilohertz quasi-periodic oscillations (kHz QPOs), then I will discuss Fourier transforms and some QPO properties. Lastly I will explain the goal of this report along with an outline of the contents for the rest of the report.

1.1 Binary neutron star systems

An X-ray binary system is a system consisting of a normal star, called the companion star, and a compact object, orbiting around a common center of mass. The compact object can be a black hole, a neutron star or a white dwarf. In such systems mass is transfered from the companion star onto the compact object by stellar winds for high-mass X-ray binaries (HMXBs, Caballero & Wilms, 2012) or by Roche-Lobe overflow which is typical for low-mass X-ray binaries (LMXBs, Frank, King & Raine, 2002). The classification between HMXBs and LMXBs depends on the type of the companion star. For HMXBs the companion star is an early-type star, i.e. a type O or B star with a typical mass of 10 $M_{\odot}$ or more, while the companion star for a LMXB is a low-mass late-type star (mass lower than 1 $M_{\odot}$, Sanna, 2013).
From this point on I will only consider LMXBs where the compact object is a neutron star since those are the objects of interest for this report. The observational data used in later Chapters is from the source 4U 1636−53 which is a neutron star LMXB source. As noted before; the accretion of matter onto the neutron star for a LMXB proceeds via Roche-Lobe overflow. This happens when the companion star fills its Roche-Lobe, which is the region in which the mass is gravitationally bound to the star. When the Roche-Lobe overflows, mass accretes from the companion star onto the neutron star through the inner Lagrange point (Frank, King & Raine, 2002).

Because the material that is falling onto the neutron star has a high angular momentum it can not directly fall onto the neutron star, but instead it spirals in forming a rotating disk. For the matter to reach the neutron star it has to lose some of its angular momentum; this can be accomplished by viscosity and friction, resulting in angular momentum moving outwards while matter moves inwards resulting in an accretion disk (Pringle & Rees, 1972). Once the accreting matter has passed the innermost stable circular object (Shakura & Sunyaev, 1973) it can freely fall onto the neutron star, emitting (mostly X-ray) radiation (Sanna, 2013). Figure 1.1 shows an artist impression of this process; we can see the companion star transferring mass to the neutron star via its Roche-Lobe and the accretion disk.

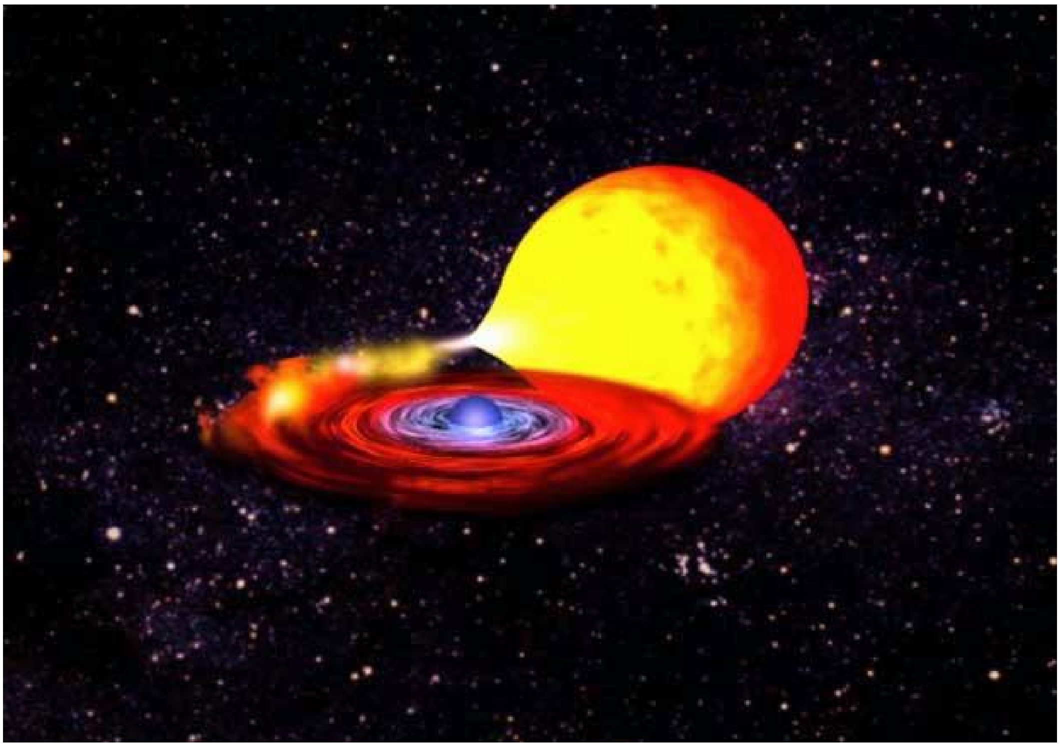

FIGURE 1.1: Artist impression of a companion star transferring mass to a neutron star (image credit:NASA)

Next to the neutron star surface and the accretion disk there is evidence for another emitting region, called the corona. The corona is a region that surrounds the neutron star and at least the inner part of the accretion disk (Sanna, 2013). Inside the corona there is a high temperature (hunderds of keV) plasma of electrons, which emits high-energy photons. There is both observational and theoretical evidence that such a plasma can interact with photons from the accretion disk via inverse Compton scattering (for example: Thorne & Price, 1975, Pozdnyakov et. al., 1983 and Dove et. al., 1997).

1.2 Kilohertz quasi-periodic oscillations

The fastest variability in any astronomical source observed so far are the kilohertz quasi-periodic oscillations (kHz QPOs). These QPOs appear in the power spectrum of LMXB neutron star systems. For these systems kHz QPOs often show up in pairs, usually called the lower and upper kHz QPO. The frequency of the QPOs depends on time. Typical QPO frequencies for neutron star LMXBs are between 400 and 1300 Hz (van der Klis 2006). Figure 1.2 shows the power spectrum of a source that has a pair of kHz QPOs.

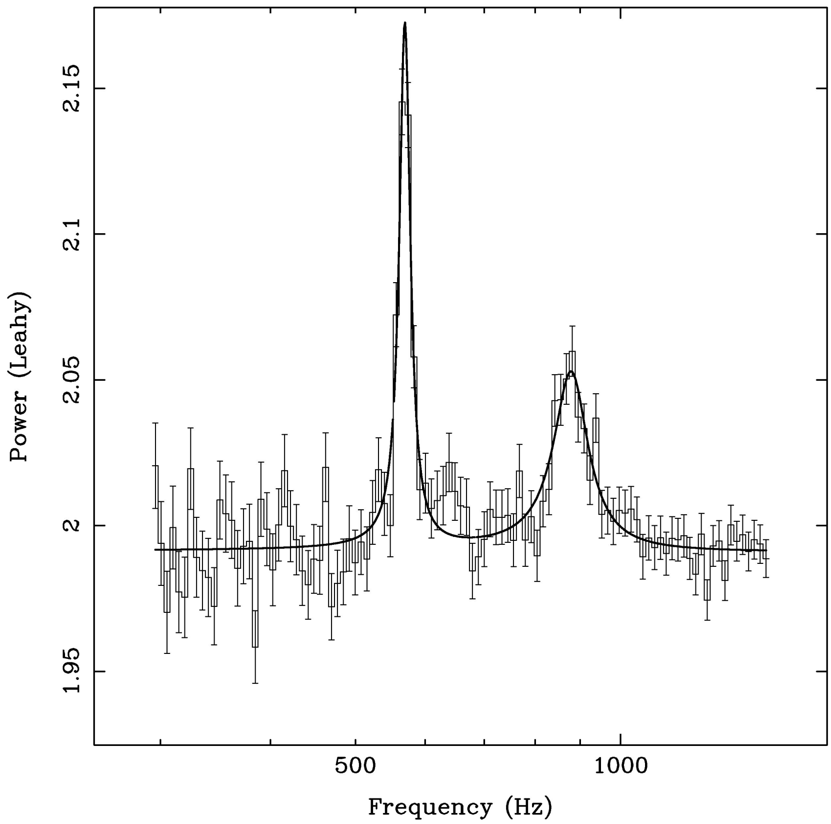

FIGURE 1.2: Example of a power spectrum that has a pair of kHz QPOs, image adopted from Méndez et. al. (1998)

Different models have been proposed to explain the kHz QPOs, for example the model discussed in Stella & Viettri (1998). These authors proposed that both kHz QPOs are due to the motion of matter inhomogeneities in the accretion disk close to the neutron star. The upper kHz QPO is then produced by Keplerian motion of matter inhomogeneities at the inner disk boundary, while the lower kHz QPO comes from periastron precession of the inner disk edge of the accretion disk. The frequency of the lower kHz QPO in this model is strongly influenced by strong-field effects. So assuming the interpretation of the kHz QPOs in this model is correct, they can be used to test strong-field general relativity (Stella & Vietri, 1998).

1.3 Fourier Transform

Fourier transforms play an important role in the study of QPO properties. The Fourier transform is a mathematical transformation which alows us to convert a series in the time domain to a series in the frequency domain and vice versa. The forward Fourier transform of a time series $f(t)$ is defined as:

$$F(\nu) = \int_{-\infty}^{\infty} f(t)e^{-2\pi i\nu t}dt, \tag{1.1}$$

while the inverse Fourier transform is define as:

$$f(t) = \int_{-\infty}^{\infty} F(\nu)e^{2\pi i\nu t}d\nu. \tag{1.2}$$

An example of a signal with kHz QPOs in the frequency domain was shown in the previous section in Figure 1.2. Here the quality factor (Q) of the QPO is defined as the frequency of the peak divided by the full width at half-maximum (FWHM). Other important quantities that are dependent on the Fourier-frequency are the time lag and coherence. These measure the time lag and linear correlation between two signals. In the case of QPOs these signals are light curves from the same source measured at two different energies (de Avellar et. al., 2013). Coherence is measured on a scale from 0 to 1, with 0 indicating that the two signals are completely uncoherent and 1 that the two signals are perfectly coherent. A coherence of 1 means that the two signals are linearly related, i.e. that there is a linear transfer function from signal 1 to signal 2 (Vaughan & Nowak, 1997). Conversely, if the coherence is not 1, there is no linear transfer function between signals 1 and 2.

Another important quantity for this report is the root mean square (RMS) of the fluctuations. The RMS is defined as the square root of the average value of the square values of a signal;

$$s_{RMS} = \sqrt{\frac{1}{n}(s_1^2 + s_2^2 + ... + s_n^2)} \tag{1.3}$$

The quantity we are interested in is the fractional rms (from here on simply called rms), which is defined as;

$$rms = \frac{s_{RMS}}{< I >}, \tag{1.4}$$

where $< I >$ is the average intensity of the signal. To calculate the Fourier transform for a discrete function one can use the discrete Fourier transform (DFT). However instead of the DFT I use the often used fast Fourier transform which is a lot quicker, especially for large arrays, by factorizing the DFT matrix. For this thesis I used the Fast Fourier Transform routines in matlab to calculate the Fourier transforms.

1.3.1 Power spectra and cross spectrum

Some interesting properties of the signal to look at are the power spectra of the individual signals and their cross spectrum. Renaming signal 1 to $x(t)$ with Fourier transform $X(\nu)$ and signal 2 to $y(t)$ with Fourier transform $Y(\nu)$, the power spectra are defined as (using the same notation as Bendat & Piersol, 1986) :

$$\begin{aligned} G_{xx} &= X(\nu)^* * X(\nu) = |X(\nu)|^2, \\ G_{yy} &= Y(\nu)^* * Y(\nu) = |Y(\nu)|^2, \end{aligned} \tag{1.5}$$

where G_{xx} is the power spectrum of x and G_{yy} is the power spectrum of y. To get the best estimate of the power spectrum one should divide the signal into shorter segments and take the FFT of each segment individually, calculate the power spectrum for this shorter duration signal and finally average over the many power spectra obtained this way instead of taking the FFT of the entire duration of the signal (Bendat & Piersol, 1986). By doing this any statistical fluctuations which might show up in a single FFT will be smoothed out. This is under the assumption that the signal is stationary.
The cross spectrum, G_{xy}, of the two signals is defined as:

$$G_{xy} = X(\nu)^* * Y(\nu) = |X(\nu)||Y(\nu)|e^{-i\phi_x(\nu)}e^{i\phi_y(\nu)} = |X(\nu)||Y(\nu)|e^{i\Delta\phi(\nu)} \tag{1.6}$$

For the cross spectrum one should take the same averaging procedure as for the power spectra discussed above.

1.3.2 Phase lags and coherence function

Two more properties to look at are the phase lag and coherence function as a function of frequency. The following relation gives the phase lag as a function of frequency, $\Delta\phi(\nu)$:

$$\Delta\phi(\nu) = arctan\left[\frac{Im(G_{xy})}{Re(G_{xy})}\right]. \tag{1.7}$$

The other property to look at is the coherence function. As mentioned before, this function determines how coherent two signals are with each other; a coherence function of 1 means that the signals are completely coherent while a coherence function of 0 means the signals are completely incoherent. The coherence function, γ^2_{xy}, is defined as (Bendat & Piersol, 1986):

$$\gamma^2_{xy}(\nu) = \frac{|< G_{xy} >|^2}{< G_{xx} > * < G_{yy} >}. \tag{1.8}$$

1.4 Research goal

The goal of this thesis is to try and create a simple model to simulate the signal from a kHz QPO to see if that can teach us something about the properties of the system. Instead of trying to create a very complicated model to simulate the observed data very closely, the idea is to keep the model simple while still getting a qualitatively good fit to the data. By keeping the model simple it takes significantly less time to explore a larger part of the parameter space. The model eventually settled on consists of just two components, a blackbody component (physically speaking this would be from the neutron star surface + the disk) and a power-law component (representing the Comptonization in the corona). Both components will contain fluctuations which are modeled by a series of shots. The observed data to which the model is compared comes from the lower kHz QPO of the source 4U 1636−53.
The rest of this report is structured as follows: Chapter 2 discusses how a single shot of the model fluctuations is constructed. Chapter 3 then discusses how I went from a single shot to creating a series of shots and how those were used as fluctuations in

the components of the model. Chapter 4 discusses how to go from one to multiple components. In Chapter 5 I try to find a theoretical relation between input and output phase lags, while in Chapter 6 I show the results of the simulations done and how they compare to the observed data. Finally in Chapter 7 I present my conclusions and I propose some options to extend the model for potential future work.

Chapter 2

Creating a shot

In this Chapter I discuss how the shots I used are created. The reason shots are used for this model instead of something else is the following; QPOs are usually fit using a Lorentzian. The FFT of a shot is also a Lorentzian, this led to the idea to model a signal that is built up of shots when investigating the properties of a QPO. Ofcourse there are other signal forms that one can take to reproduce the Lorentzian-like feature in the power spectrum. The choice for shots was made because of its simplicity, while still being able to explore the basic properties of a signal that is consistent with the observed data.

2.1 Shot form

I started of by creating shots for two signals of the form:

$$\begin{aligned} S_1 &= B_1 + A_1 e^{-t/\tau} sin(2\pi\nu_0 t + \phi_1), \\ S_2 &= B_2 + A_2 e^{-t/\tau} sin(2\pi\nu_0 t + \phi_2), \end{aligned} \tag{2.1}$$

where the phase lag, $\Delta\phi = \phi_2 - \phi_1$, and τ (which determines the rate at which the sine is damped) are taken from the literature for a certain frequency ν_0. B_1 and B_2 determine the average value of the signal, which can be changed according to the case one is looking at. The amplitudes A_1 and A_2 determine the size of the fluctuations of the signal, again the values of these can change depending on the case considered.

2.1.1 Phase lag

The phase of the first signal, ϕ_1, is taken to be 0. Then the phase of the second signal, ϕ_2, is simply equal to the phase lag, $\Delta\phi$. The observed phase lag is taken from de Avellar et al. (2013). Their Figure 3 (Figure 2.1) shows the time lag between photons from 2 different energy bands as a function of QPO frequency. Taking the data points in this figure (for the lower kHz QPO of the source 4U 1636−53) and using fitting routines from matlab, a relation between the QPO frequency, ν_0, and time lag, Δt, was obtained. Then using the following relation the phase lag can be obtained:

$$\Delta t = \frac{\Delta\phi}{2\pi\nu_0}. \tag{2.2}$$

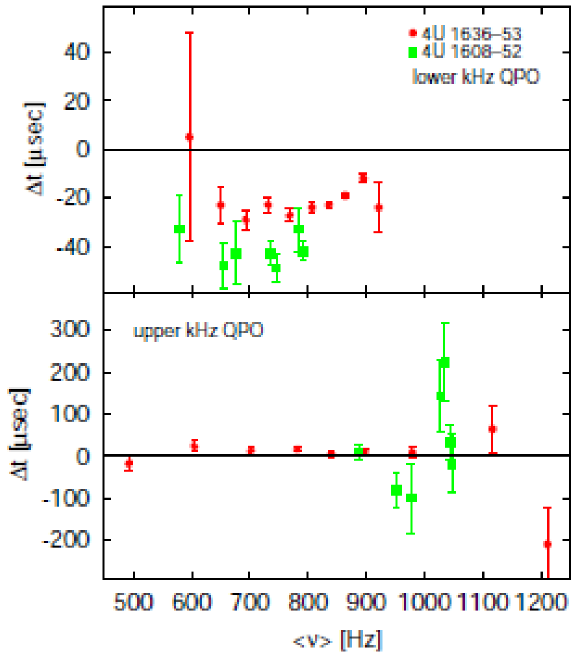

FIGURE 2.1: Figure 3 from the Avellar et al. (2013), showing the time lag of the kHz QPOs in two sources as a function of the frequency. For this thesis I used the data for the lower kHz QPO of the source 4U 1636−53.

2.1.2 Tau

The decay timescale of the shots, τ, as a function of frequency was obtained from Barret et. al. (2006). Their Figure 2 (Figure 2.2) shows the quality factor, Q, as a function of QPO frequency, again taking the data points for the lower kHz QPO of source 4U 1636−53. Fitting a function to these data points gives the value of Q for a given frequency. The value of τ can then be obtained using the following relation between Q and

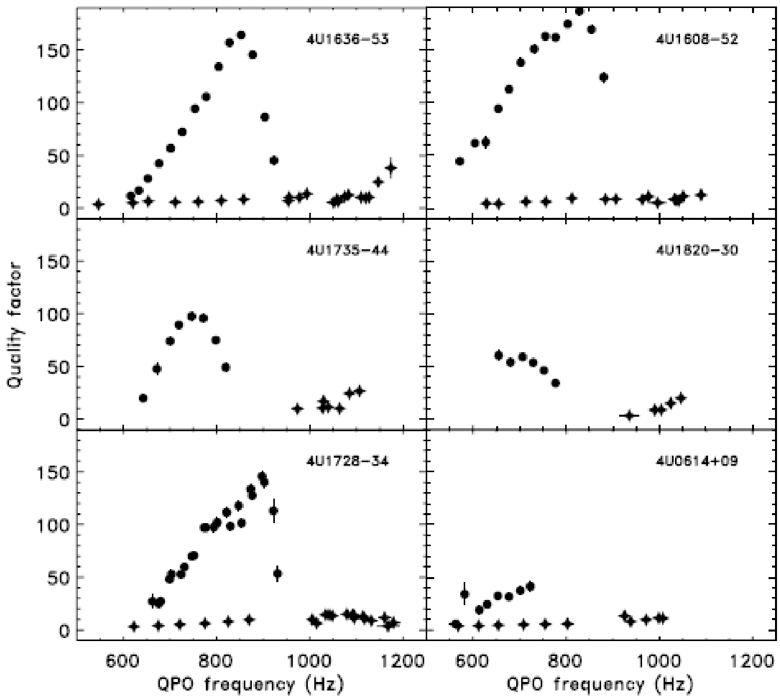

FIGURE 2.2: Figure 2 from Barret et al. (2006), showing the quality factor, Q, of the kHz QPOs in six sources as a function of the QPO frequency. I used the data for the lower kHz QPO of the source 4U 1636−53.

τ (van der Klis, 1989):

$$\tau = \frac{Q}{\pi \nu_0}. \tag{2.3}$$

2.1.3 Amplitude

The amplitudes A_1 and A_2 determine the size of the fluctuations in the signal; these can set according to the case one wants to consider. For example, in some cases it is desirable to keep the fluctuations small to make sure the signal will not become negative. Another option is to take the amplitude as a free parameter to see which amplitude value best reproduces the observed data.

2.2 Single shot

Once the form of the signal was completely defined the first thing to look at was signals consisting of just a single shot at a given frequency, in this case $\nu_0 = 800$ Hz. Figure 2.3 shows what such a signal looks like; as expected it is just a simple damped sinusoid.

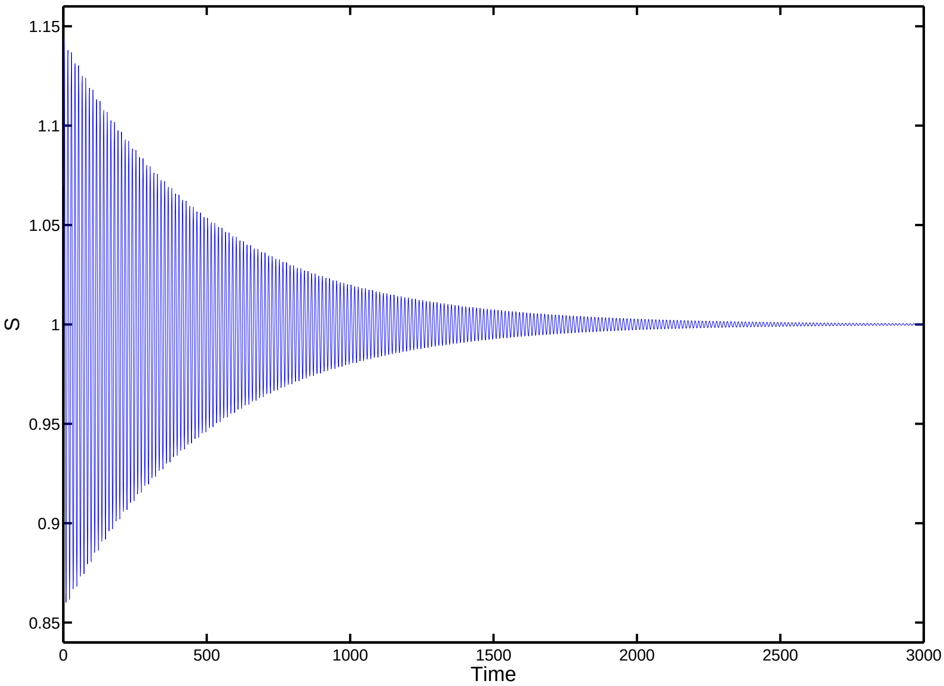

FIGURE 2.3: Single shot of the form $S = B + Ae^{-t/\tau}sin(2\pi\nu_0 t + \phi)$. Units in this Figure are arbitrary, since it only serves to show the shape of the signal.

Figure 2.4 shows the power spectra, cross spectrum, phase lag and coherence function as a function of frequency of two signals which both consist of a single shot. The power spectra and cross spectrum show a single peak at 800 Hz, which is to be expected since the signal consists of just one component at that frequency. The phase lag shows a strange behaviour. This might be an artifact of the fact that these signals consist only of a single shot. The value for the phase lag at 800 Hz is the same as the one taken from the plot in de Avellar et al. (2013). The coherence function is 1 for every frequency, which was to be expected since the coherence function considers averages while here only one sample was used; to get a meaningful plot for the coherence function one has to sample over many FFT's (see section 1.3).

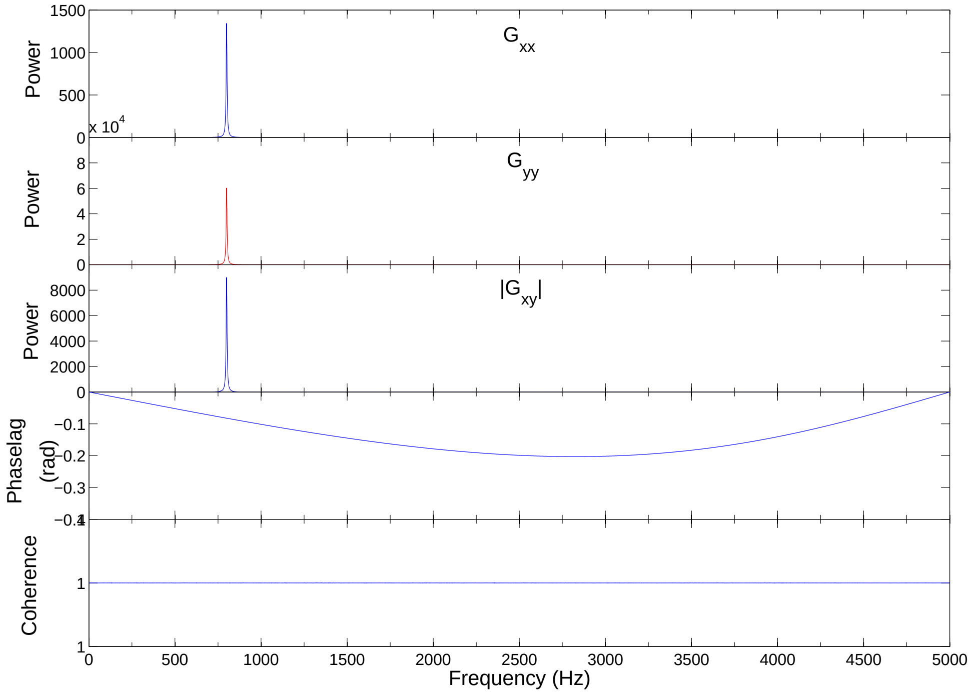

FIGURE 2.4: The power spectra, the cross spectrum, the phase lags and the coherence function as a function of frequency of two signals consisting of a single shot. The units for the power spectra and cross spectrum in this and any following plots are $(\frac{counts}{Hz})^2$.

Chapter 3

Creating many shots

3.1 Summation of many shots

The next step is to look at signals that consist of a series of shots summed together. In this section I first describe how these signals have been built up and then proceed to look at a number of different scenarios using these signals.

3.1.1 Constructing the signal

The first thing to consider when creating a signal that is a summation of shots is when to let each individual shot start. It seems obvious to take random starting times from some kind of distribution. The first shot starts at $t = 0$, then a Δt_1 is determined randomly and the start time of the second shot is set at $t = \Delta t_1$. A new Δt_2 is drawn and the third shot starts at $t = \Delta t_1 + \Delta t_2$ and so on until the total length of the observation is filled. Since the measuring process in X-ray Astronomy is Poissonian (counting photons), the starting time of the shots should be a Poisson process. This means the $\Delta t's$ should be drawn from an exponential distribution, since that describes the time between events in a Poisson process. The start times for the shots in both signals are the same at this time.

When considering a signal consisting of a single shot, the first signal had a phase of 0 and the second signal a phase equal to the phase lag taken from de Avellar et al. (2013). However, for a real source not every shot will have a phase of 0; I therefore assumed that the phases of these shots follow a uniform distribution between 0 and 2π. This means that for every shot in the first signal a random phase between 0 and 2π is assigned; the second signal then has a phase equal to that random phase from the first signal plus the phase lag taken from de Avellar et al. (2013). All this leaves us with signals of the form:

$$S_1 = B_1 + \Sigma_{i=1}^{N}\ A_1 e^{-t_i/\tau} sin(2\pi\nu_0 t_i + \phi_{i,1}),$$
$$S_2 = B_2 + \Sigma_{i=1}^{N}\ A_2 e^{-t_i/\tau} sin(2\pi\nu_0 t_i + \phi_{i,2}), \tag{3.1}$$

where the shot starting times and phases are defined as above and the amplitudes, τ and frequency are constant between shots. Figure 3.1 shows what such a signal looks like.

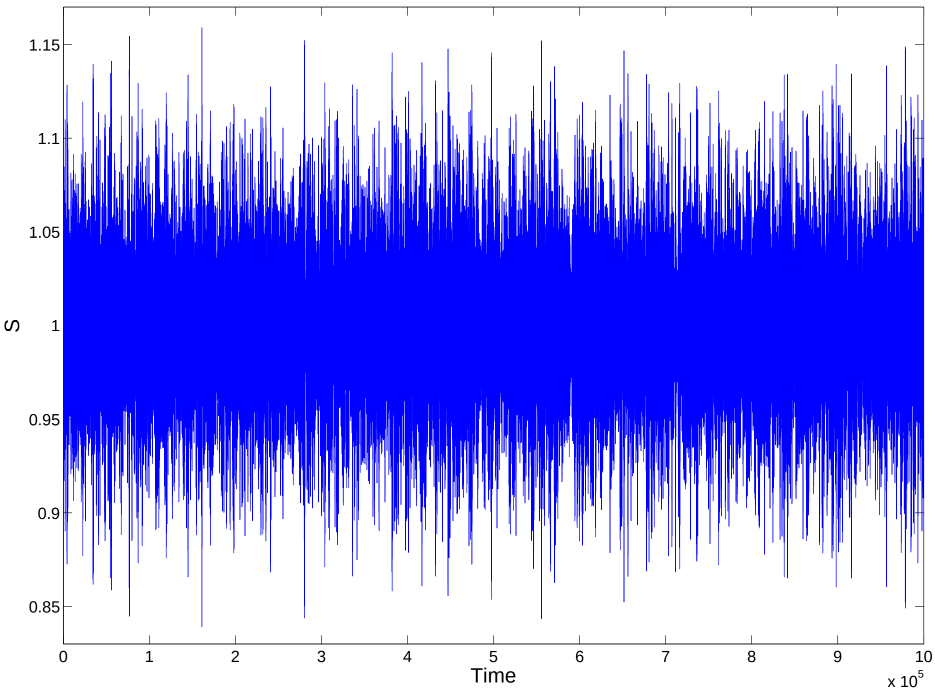

FIGURE 3.1: A signal that is a summation of many shots, as given in equation 3.1. Units in this Figure are arbitrary, since it only serves to show the shape of the signal.

3.1.2 Fourier power and cross spectra, phase lags and coherence

Instead of taking a single FFT of the entire signal, as done in the single shot case, the average of many shorter FFTs should be taken to get the best estimate of the power and cross spectra and a meaningful value for the coherence function (see section 1.3). This is done by taking the entire time range of the signal and dividing it into a number of equal length segments (in this case 128 segments of 6.55 seconds each), the FFT of each segment is taken individually. The first few seconds of the shot series are not used because the shots have not had time to build up, i.e. we would be looking at a part of the signal where there is only a single shot, then a part with only two shots, etc. After some time the amount of shots summed will be more or less constant at any given time because of the way they are generated and damped. This is the part of the signal I am interested in. These FFTs are used to calculate the average power and cross spectrum. Doing all this for the signal described in the previous subsection gives the results shown in Figure 3.2. In this Figure we can see that the power spectra and the cross spectrum only show peaks at 800 Hz (ν_0), which is to be expected since the shots of which the signal is composed all have a frequency of 800 Hz. In the phase lag plot we can see that it is flat at frequencies around 800 Hz; there the phase lag has the value which was taken from the plot in de Avellar et al. (2013), which was the input in our shots. Around 800 Hz the phase lag also has the smallest fluctuations, which makes sense since that is the only frequency around which the signal has power, so for other frequencies the phase lag will not be well constrained. We can see a similar trend in the coherence plot, where the coherence is 1 around a frequency of 800 Hz and drops off for frequency values moving away from 800 Hz. The coherence at 800 Hz is expected to be 1 since the shots used for both signals are very similar, the only difference being the amplitudes and the phases.

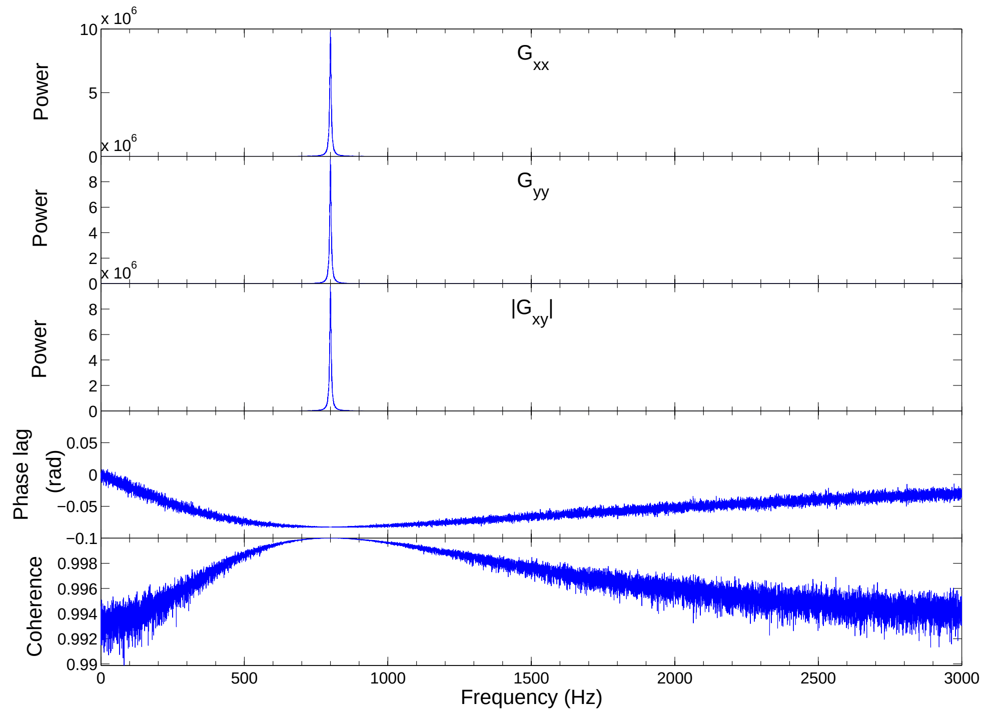

FIGURE 3.2: Plot showing the power spectra, cross spectrum, phase lag and coherence function for the signal described in section 3.1

3.2 Temperature shots

The first scenario I considered was based on the ideas of Vaughan & Nowak (1997); they explored the case in which the variability might be the result of local temperature fluctuations which depend on time. To simulate this I took a signal consisting of shots of these temperature fluctuations $kT(t)$. I took an average kT of 2 keV (B_1 in equation 3.1) and an amplitude of 0.03 keV (A_1 in equation 3.1). This value for the amplitude was chosen to make sure the fluctuations in temperature are small. I then used the blackbody formula (below) to get the final signal.

$$S = N_{BB} * \frac{E^2}{e^{E/kT(t)} - 1}, \tag{3.2}$$

where E is the energy of the signal and N_{BB} is a normalization constant which I take to be 1 at the moment (can easily be rescaled later). After creating $kT(t)$ I took 2 different energies (E_1 and E_2), calculated the blackbodies at those energies and looked if they were coherent. I looked at different scenarios: the first one is where both energies are a lot smaller than $< kT >$. Figure 3.3 shows the power and cross spectra, phase lag and coherence for $E_1 = 0.5$ keV and $E_2 = 1$ keV. In this case we are in the Rayleigh-Jeans regime and, as noted in Vaughan & Nowak (1997), we expect the coherence to be 1, which is what is reproduced in this Figure. Note that the phase lag is 0, this is expected because we do not put in a phase lag in this case; the blackbodies at the two energies use the same temperature fluctuations, which means they have the same phase. There is something strange happening at 1600 Hz, for which I do not have an explanation yet, but seems to be some kind of artifact. If we consider higher energies; $E_1 = 5$ keV and $E_2 = 10$ keV we can see a very similar thing happening (Figure 3.4), except in this case the unexplained feature at 1600 Hz is stronger. If we look at even higher energies, $E_1 = 50$ keV and $E_2 = 100$ keV we see in Figure 3.5 that the coherence has dropped significantly. This is what is predicted in Vaughan & Nowak (1997) because we are now in the Wien regime.

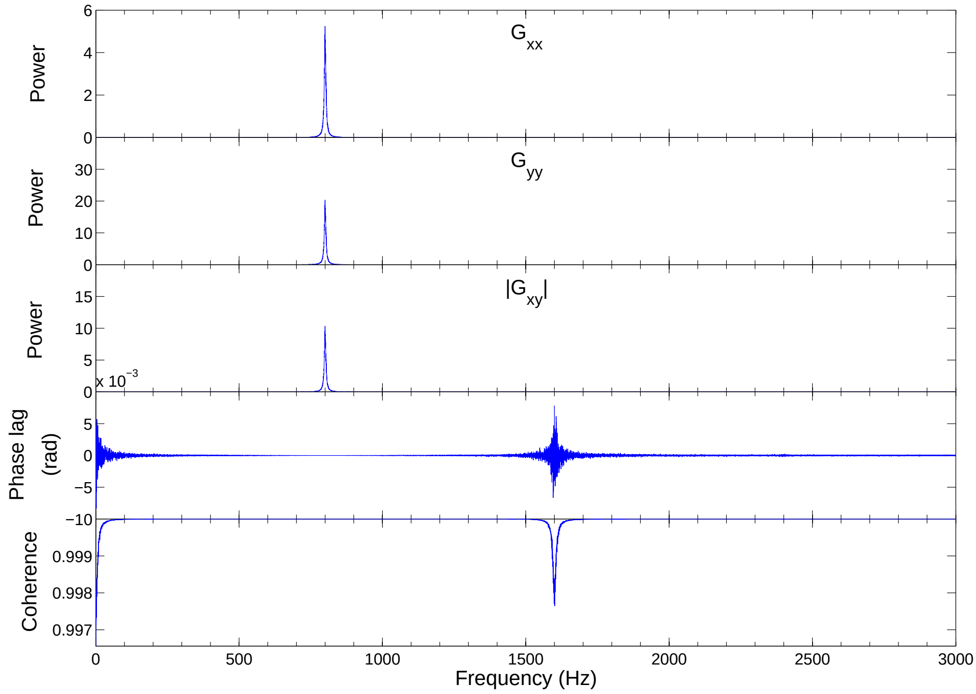

FIGURE 3.3: Plot showing the power spectra, cross spectrum, phase lag and coherence function for the temperature shots signal with $E_1 = 0.5$ keV and $E_2 = 1$ keV.

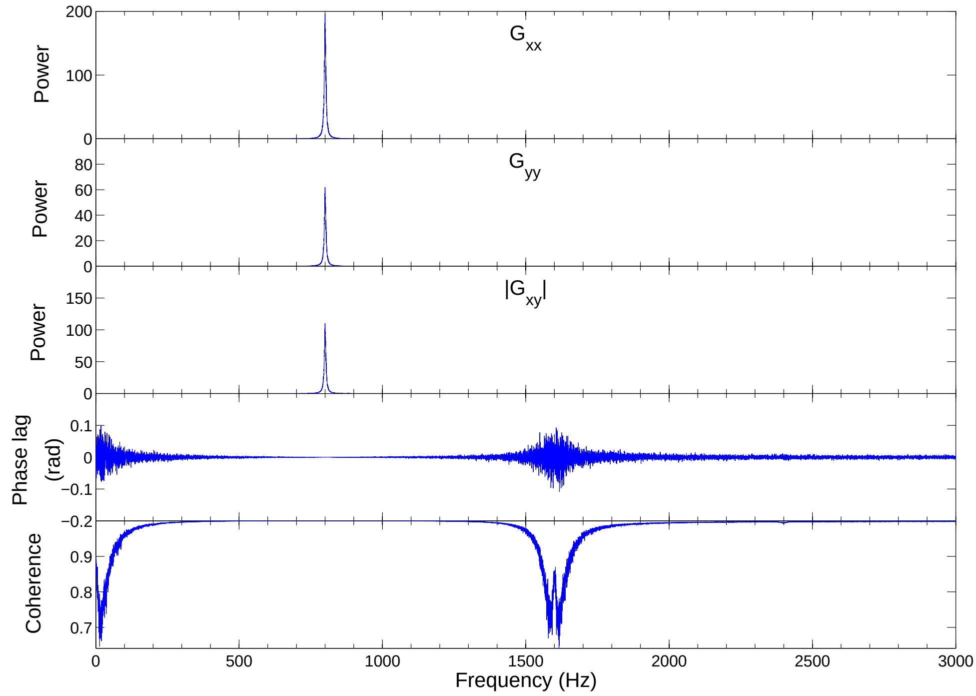

FIGURE 3.4: Plot showing the power spectra, cross spectrum, phase lag and coherence function for the temperature shots signal with $E_1 = 5$ keV and $E_2 = 10$ keV.

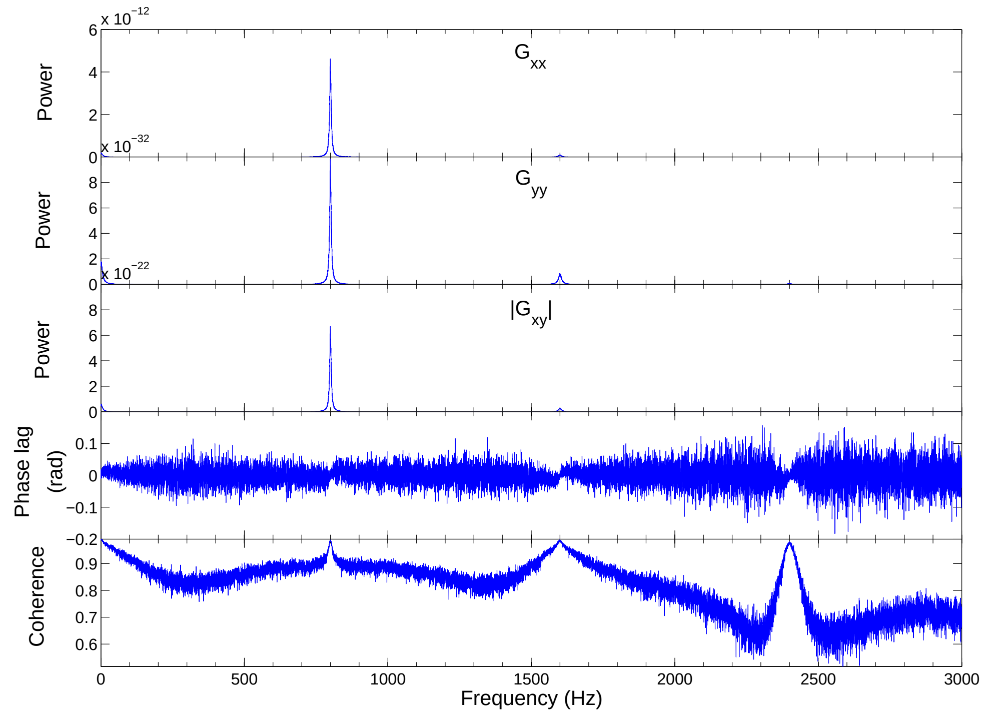

FIGURE 3.5: Plot showing the power spectra, cross spectrum, phase lag and coherence function for the temperature shots signal with $E_1 = 50$ keV and $E_2 = 100$ keV.

3.3 Power law shots

In a similar vein to the previous section I also tried using a shot series as fluctuations in a power law. Here the shots were taken as $\Gamma(t)$ in the power-law formula (below). I took an average Γ of 2 and chose for an amplitude of 0.03 again to ensure that the fluctuations in Γ remained small:

$$S = N_{PL} * E^{-\Gamma(t)}, \tag{3.3}$$

where N_{PL} is a normalization constant (which I take to be 1 at the moment, but can be easily rescaled later if needed). Again I looked at different energies. In this case for the low-energy case I looked at $E_1 = 0.5$ keV and $E_2 = 1.1$ keV. We can not take $E_2 = 1$ keV because of the way the power law is defined, we would always get $S = 1$ for any Γ if we take $E = 1$ in equation 3.3. So instead I just took a value slightly larger than 1. We can see in Figure 3.6 that the phase lag is again 0, because we did not put any phase lag in. We can see the coherence is 1 everywhere except for frequencies around 1600 Hz where the coherence drops to 0. Similar to the blackbody case I do not know why this is happening. If we look at the intermediate energies ($E_1 = 5$ keV and $E_2 = 10$ keV) in Figure 3.7 we see similar things happening at 1600 Hz and 2400 Hz; the features are much shallower than in the low-energy case, though. For the high-energy case (with $E_1 = 50$ keV and $E_2 = 100$ keV), in Figure 3.8 we again see similar things but with small differences: the features are a lot shallower here than in the low energy case, but here the feature at 2400 Hz is more pronounced than the feature at 1600 Hz (contrary to the previous plot). In conclusion; something strange is happening at the harmonics of the signal, but so far I did not figure out where this is coming from.

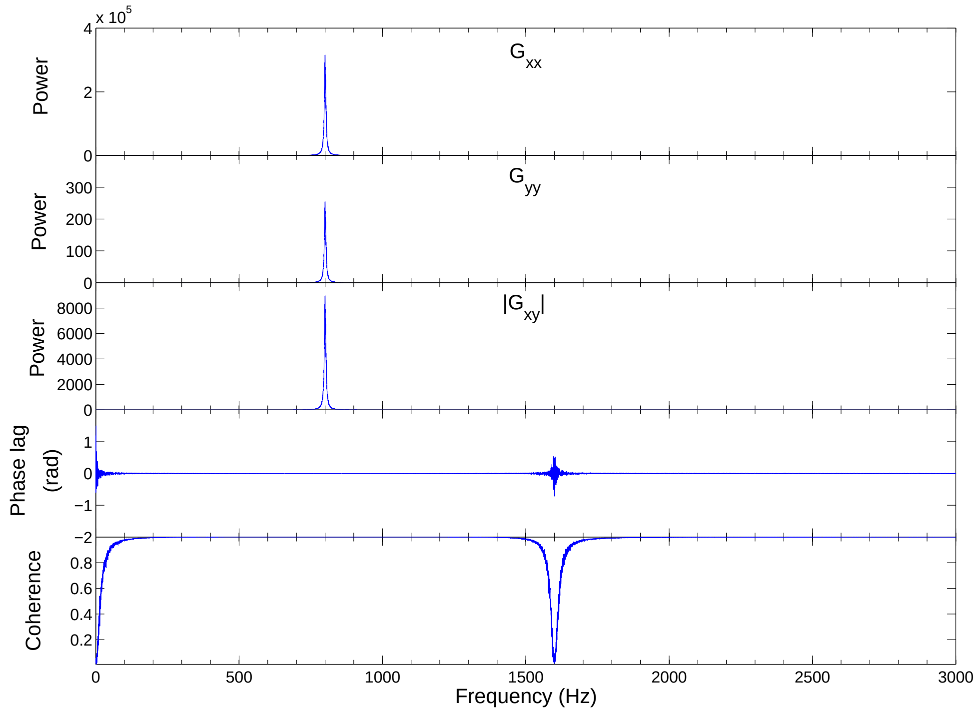

Figure 3.6: Plot showing the power spectra, cross spectrum, phase lag and coherence function for the power-law shots signal with $E_1 = 0.5$ keV and $E_2 = 1.1$ keV.

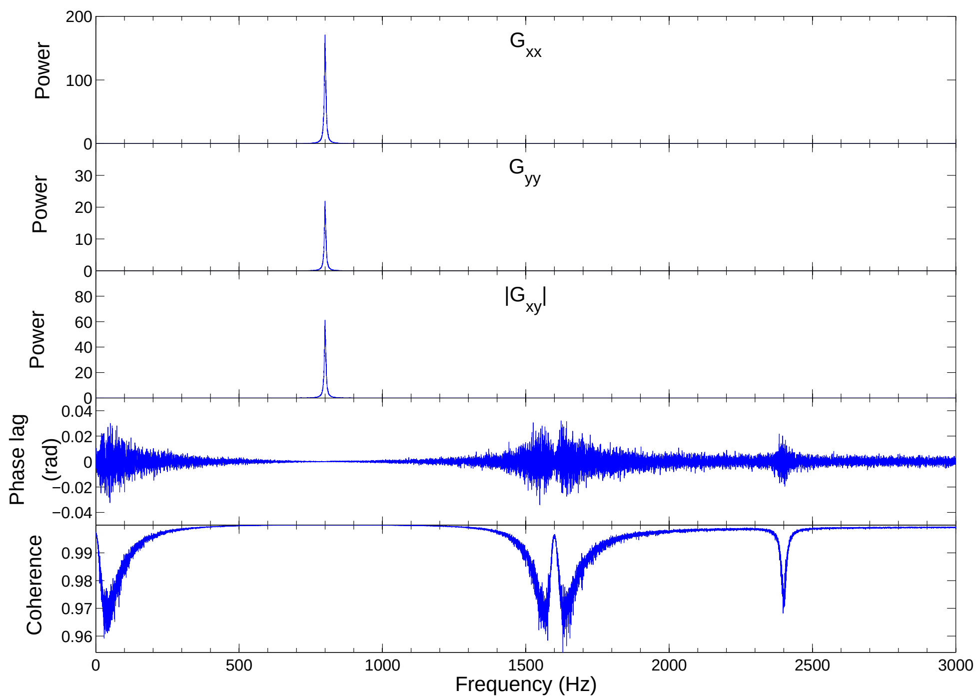

Figure 3.7: Plot showing the power spectra, cross spectrum, phase lag and coherence function for the power-law shots signal with $E_1 = 5$ keV and $E_2 = 10$ keV.

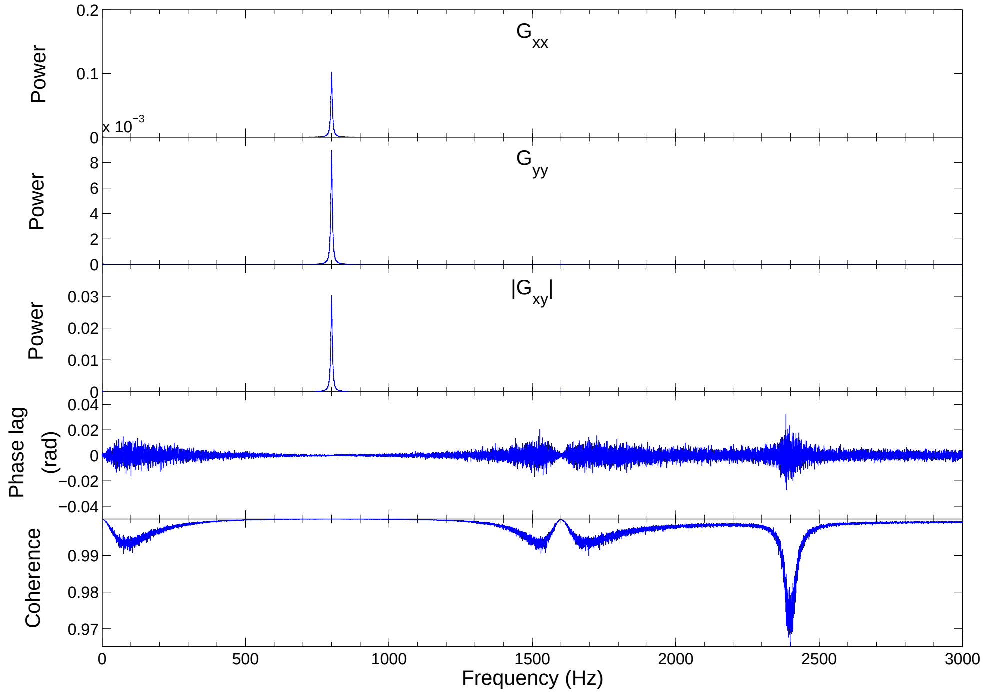

FIGURE 3.8: Plot showing the power spectra, cross spectrum, phase lag and coherence function for the power-law shots signal with $E_1 = 50$ keV and $E_2 = 100$ keV.

Chapter 4

Multiple regions

In previous Chapters I always considered signals consisting of only a single component, but in fact the signals are likely to have multiple components which originate in different regions, for example the neutron star surface, the disk or the corona. In this section I study signals that consist of two components, namely a blackbody and a power-law component, which may physically be attributed to photons emmited from the neutron star surface and the Comptonization of photons in the corona, respectively.

4.1 General concept

Assume there are two regions contributing to the final signal, bb and pl. Then region bb produces a timeseries: $bb(t) = bb_1(t) + bb_2(t)$ while region pl produces a timeseries: $pl(t) = pl_1(t) + pl_2(t)$. The subscripts 1 and 2 stand for two different energies. If we observe these regions, what we will see is two signals at energies E_1 and E_2 which are built up as: $s_1(t) = bb_1(t) + pl_1(t)$ and $s_2(t) = bb_2(t) + pl_2(t)$. These signals do not need to be coherent even if $bb_1(t)$ and $bb_2(t)$ are coherent with each other and $pl_1(t)$ and $pl_2(t)$ are coherent with each other (Vaughan & Nowak 1997). From a physical point of view we expect these components to be related in some way. There are many ways to go about this, but the two ways I considered here are as follows:

a.) Taking a shot series as fluctuations for the blackbody component and using a time-shifted version of this shot series as the fluctuations for the power law. I call this 'strongly' related from now on.

b.) Creating two shot series with a phase lag $\Delta\phi$ between them and using one of them as the fluctuations for the blackbody component and the other for the fluctuation in the power-law component. I will call this 'weakly' related from now on.

Note that strongly and weakly related in this case are not based on a clear-cut criterium, rather the names just serve to avoid confusion between the two cases I consider in this Chapter.

In both cases the two signals will have the following form:

$$
\begin{aligned}
S_1 &= z \times \frac{E_1^2}{e^{E_1/kT(t)} - 1} + E_1^{-\Gamma(t)}, \\
S_2 &= z \times \frac{E_2^2}{e^{E_2/kT(t)} - 1} + E_2^{-\Gamma(t)},
\end{aligned}
\tag{4.1}
$$

where $kT(t)$ and $\Gamma(t)$ are series of shots and z determines the relative contribution of the blackbody and power-law components ($z = N_{BB}/N_{\Gamma}$).

4.2 Strongly related regions

In the strongly related case the shot series that I used as the fluctuations in the power-law component is simply a time-shifted version of the fluctuations used for the blackbody component. What this means is that I took the array that holds the shot series for the blackbody and simply shift it by a number of points depending on how large a time delay (δt) I want to consider. Figure 4.1 shows the power spectra, cross spectrum, phase lag and coherence as functions of frequency for $E_1 = 5$ keV, $E_2 = 10$ keV and $\delta t = 0.1s$. All the panels in this Figure show a comb-like structure (best seen in the bottom 2 panels). The separation between two lines in the 'comb' is determined by the value taken for δt; a δt of 0.1 seconds gives a separation of $1/0.1 = 10$ Hz. I have also looked at different energy pairs, but each one produces the same comb-like behaviour shown in Figure 4.1. It turns out that simply shifting the shot series and using that as the fluctuations in the power-law component produces this aliasing, making it not really a useful scenario to consider further.

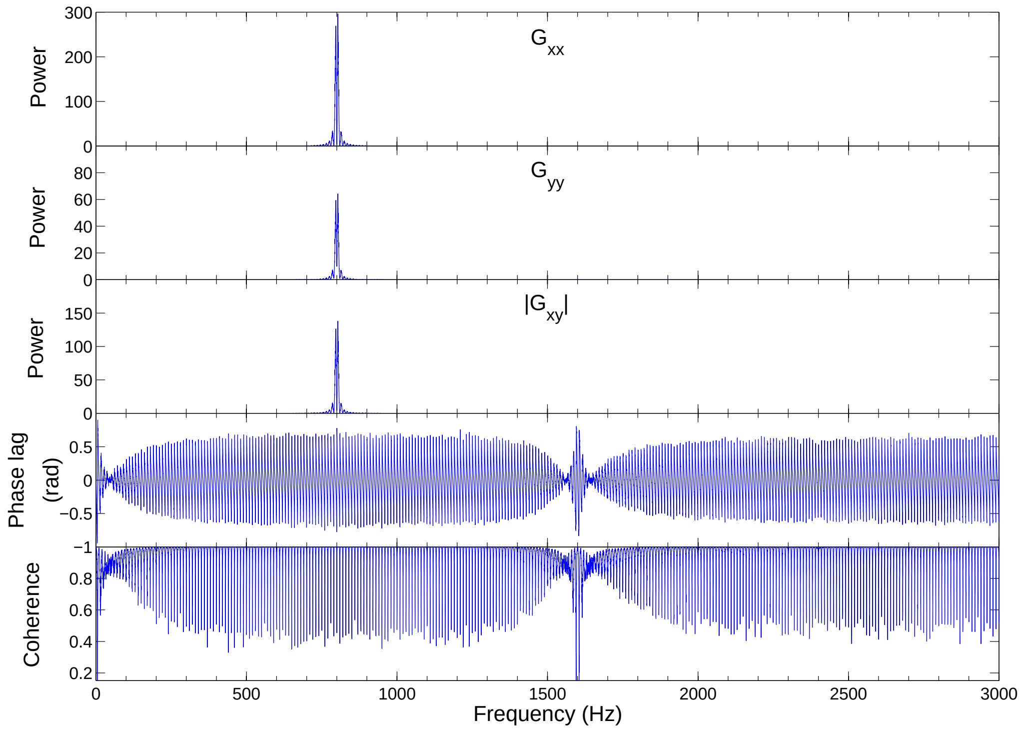

FIGURE 4.1: Strongly related regions show a comb structure, $E_1 = 5$ keV and $E_2 = 10$ keV.

4.3 Weakly related regions

In the second case I considered two shot series with a phase lag $\Delta\phi$, where the first series of shots is used as the temperature fluctuations, $kT(t)$, in a blackbody component and the second series is used as fluctuations in $\Gamma(t)$ in a power-law component. The phase lag used as input is taken form de Avellar et al. (2013) as before; the value of the phase lag from their plot at 800 Hz is $\Delta\phi = -0.0825$ rad. For the average temperature ,$< kT >$, and average Γ ,$< \Gamma >$, I take a value of 2 for both and the amplitudes for the shot series are taken to be: $A_{kT} = 0.03$ and $A_\Gamma = 0.03$ (A_1 and A_2 in equation 3.1) to make sure fluctuations remain small. The value for z for 4U 1636−53 is obtained from Sanna et al. (2013): $z = 0.022$.
Figures 4.2 and 4.3 show the power spectra, cross spectrum, phase lags and coherence function for two pairs of such signals. Figure 4.2 compares signals at energies $E_1 = 5$ keV and $E_2 = 10$ keV, while Figure 4.3 compares signals at $E_1 = 2$ keV and $E_2 = 20$ keV. As we can immediately see the two Figures are very different; this has to do with the energy pairs that have been taken, since at different energies the contributions of the blackbody and power-law components change. At low and high energies the power law dominates, while at intermediate energies the blackbody slightly dominates.

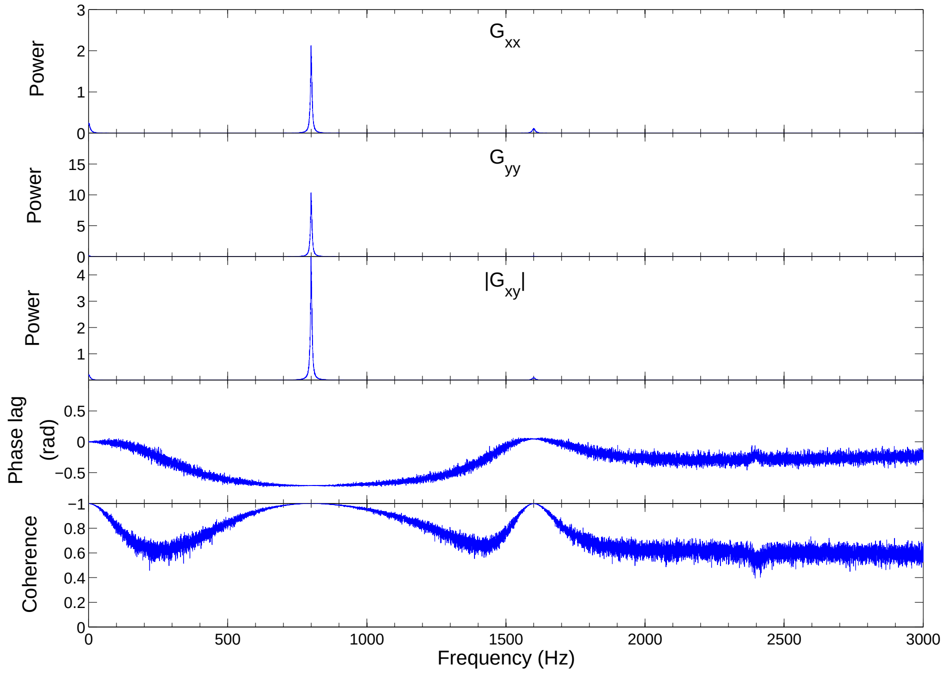

FIGURE 4.2: Plots considering the weakly related regions case for energies $E_1 = 5$ keV and $E_2 = 10$ keV.

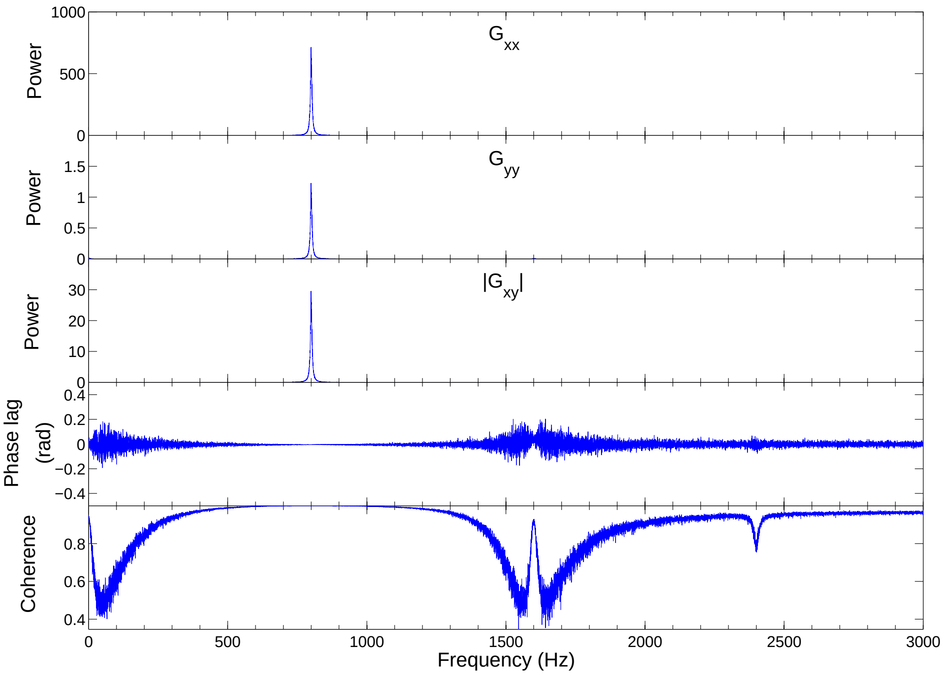

FIGURE 4.3: Plots considering the weakly related regions case for energies $E_1 = 2$ keV and $E_2 = 20$ keV.

This is very clear in Figure 4.3, which looks very similar to Figure 3.7. This is because we are considering two energies at which the power-law component is much larger than the blackbody component, meaning we are effectively just looking at a signal with only one component as in Figure 3.7. Another thing to note is that the measured phase lags at 800 Hz are different in both plots, neither of which is equal to the input phase lag. But this is to be expected since we are looking at signals of the form:

$$\begin{aligned} S_1 &= BB_1(\phi_1) + PL_1(\phi_2), \\ S_2 &= BB_2(\phi_1) + PL_2(\phi_2), \end{aligned} \tag{4.2}$$

where BB_1 and PL_1 are the blackbody and the power law at energy 1, respectively, and BB_2 and PL_2 are the blackbody and the power law at energy 2, respectively, ϕ_1 is the phase of the shot series used for the blackbody and ϕ_2 is the phase of the shot series used for the power law. The input phase lag is then $\delta\phi = \phi_2 - \phi_1$ while the phase lag in the figures, which is the one we are interested in, is the phase lag between signals 1 and 2, i.e., $\Delta\phi = \phi_{S2} - \phi_{S1}$. It is clear that these need not be the same in most cases.
Ideally one would like to find a relation between $\delta\phi$ and $\Delta\phi$. In the next Chapter I explore whether there exists a simple relation between the two for the two-component model used here.

Chapter 5

Lags

In this Chapter I try to find a relation between $\delta\phi$ (the phase lag between the blackbody and power-law components) and $\Delta\phi$ (the phase lag between two signals at two different energies). First I will look at the intrinsic lags of the individual components of the model, then I will try to find a relation between $\delta\phi$ and $\Delta\phi$ by starting from the simple case of adding two sine functions, and finally I will extend that simple case to the one of the two-component model presented here.

5.1 Intrinsic lags of individual components

In general, the individual components of a signal can have an intrinsic lag (see for example Kara et. al. 2013a), which may have an effect on the lags of the signal as a whole. The goal of Kara et. al. (2013a) is to study lag measurements in an AGN. To this end they make simulations to check whether the observed lags are equal to the intrinsic lag for different scenarios (Kara et. al 2013b). They created simulated light curves from a red-noise power spectrum and studied what the effects of different kinds of contamination of the signal are on the measured lag. They find that if the signal is a combination of two varying components, the lag will simply be a weighted contribution from both those components. In Kara et. al. (2013a) they conclude that if there is no contamination between the components, the measured lag will be equal to the intrinsic lag, while in the case that both bands have equal parts of both components the measured lag will be 0. However we should consider that we are looking at a completely different frequency range (order 10^{-3} Hz versus order 10^{3} Hz). In the frequency range which we are interested in ($\sim 400-1200$ Hz) the contribution from the red-noise power spectrum is basically zero, at those frequencies we have QPOs on top of a Poisson noise spectrum (see e.g., Figure 1.2, adopted from Méndez et. al. 1998). Kara et. al (2013b) show that additive Poisson noise does not change the measured lag of that signal. So in our case we do not expect to find intrinsic lags for an individual component around the frequency of the QPO (in this case 800 Hz). In the next subsections I explore whether this expactation holds or not.

5.1.1 Blackbody

To check for intrinsic lags of the blackbody component I looked at three different cases:

1.) The blackbody has a fixed N_{BB} and a variable kT.
2.) The blackbody has a variable N_{BB} and a constant kT.
3.) The blackbody has both a variable N_{BB} and kT, but the variable parameters are related.

The first case, where N_{BB} is constant and a series of shots is used to create the temperature fluctuations in kT has been described in section 3.2, where we saw that the phase lag at 800 Hz is 0, independent of the two energies considered. The second case, where instead of using the shot series as fluctuations in kT they are used as fluctuations in N_{BB} gives a phase lag of 0 at all frequencies for any pair of energies. This makes sense, since we are only changing the normalization in this case, which just shifts the blackbody up or down but has no influence on the phase lag. In the third case the shot series is taken as fluctuations in kT again, but in this case N_{BB} is given by $N_{BB} = c_1 \times kT + c_2$, with c_1 and c_2 constants; this ensures that N_{BB} increases (decreases) when kT increases (decreases) as long as $c_1 > 0$. The reason to take $c_1 > 0$ is that in previous work (albeit on longer time scales) shows that in these systems the blackbody normalization and temperature are correlated (Sobczak et. al. 1999). This case also gives 0 phase lag around 800 Hz, independent of the c_1, c_2 and energies chosen. An example of this case is shown in Figure 5.1.

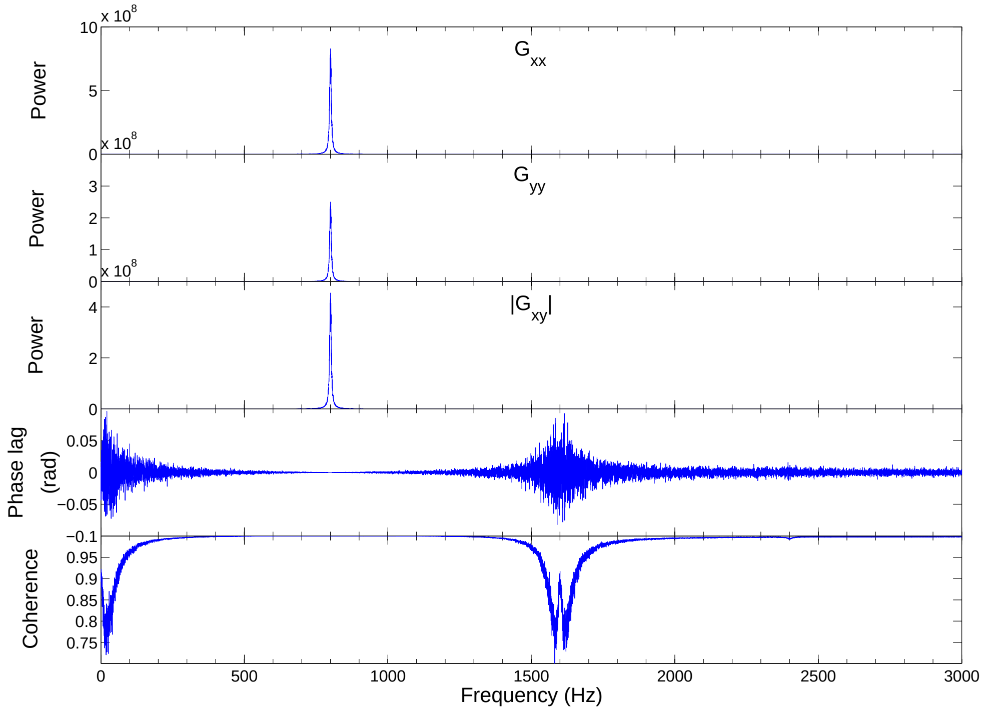

FIGURE 5.1: Example plot for the intrinsic lags of a blackbody with variable N_{BB} and Γ (E_1=5 keV and E_2=10 keV, $c_1 = 3$, $c_2 = 40$).

5.1.2 Power law

To check for intrinsic lags of the power-law component I also looked at three different cases, as in the previous section:

1.) The power law has a fixed N_{PL} and a variable Γ.
2.) The power law has a variable N_{PL} and a constant Γ.
3.) The power law has both a variable N_{PL} and Γ, but the variable parameters are related.

The first case has been described in section 3.3; the plots in that section show that the phase lags around 800 Hz are always 0, independent of the two energies considered. For the second case, instead of using a shot series to model the fluctuations in Γ, Γ is taken as a constant, while N_{PL} is fluctuating as opposed to being constant. This gives a phase lag of 0 at every frequency for any pair of energies considered. Again this result makes sense, since we are only changing the normalization which does not affect the phase lag. The third case consideres fluctuations in Γ again, but also has fluctuations in N_{PL} following the relation $N_{PL} = -c_1 * kT + c_2$ with c_1 and c_2 constants. Similar to the case of the blackbody emission in these systems the power-law index and normalization are anticorrelated on long timescales (Sobczak et. al. 1999). In this case the phase lag around 800 Hz is always 0 as well, independent of the c_1, c_2 and energies chosen. An example of this is shown in Figure 5.2.

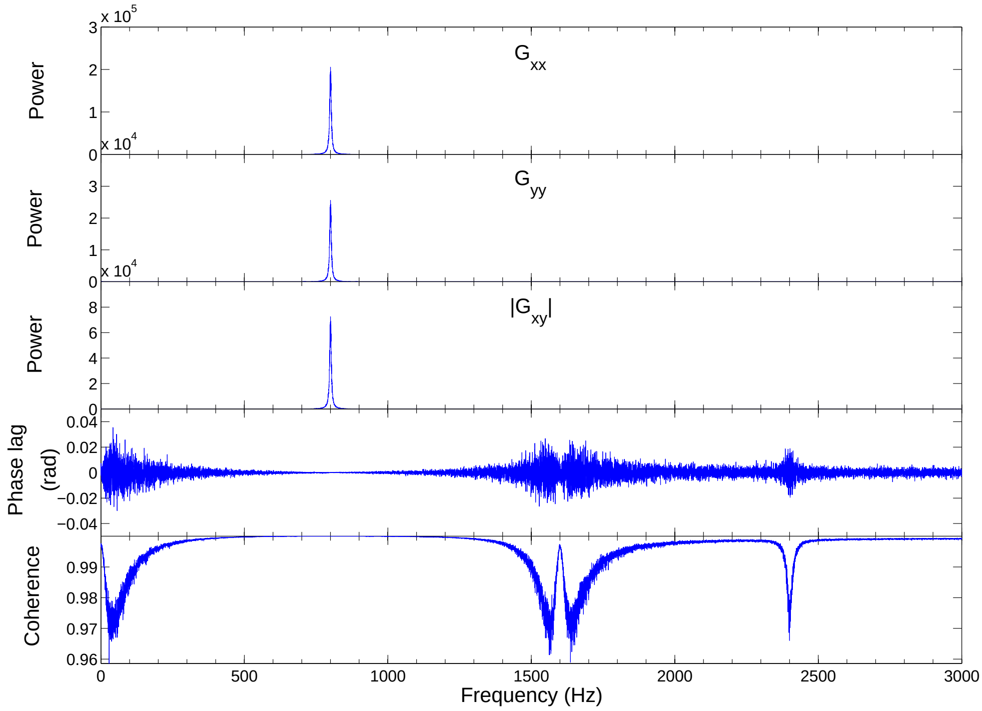

FIGURE 5.2: Example plot for the intrinsic lags of a power law with variable N_{PL} and Γ (E_1=5 keV and E_2=10 keV, $c_1 = 3$, $c_2 = 40$)

5.1.3 Conclusion on intrinsic lags

The expectation was that the blackbody and power-law components would not have an intrinsic lag for the frequencies of interest. The previous two subsections confirmed this expectation.

5.2 Lags for the two component model

In this section I try to find a relation between $\delta\phi$ and $\Delta\phi$ by starting out with the simple case of adding two sine functions and comparing that to the more complicated two-component model introduced in Chapter 4.

5.2.1 Simplified case: addition of two sine waves

For the simpler case where we are just adding two sine waves we have the relation:

$$\begin{aligned} Asin(\omega t+\alpha)+Bsin(\omega t+\beta) &= \sqrt{[Acos(\alpha)+Bcos(\beta)]^2+[Asin(\alpha)+Bsin(\beta)]^2} \\ &\times sin(\omega t + arctan\left[\frac{Asin(\alpha)+Bsin(\beta)}{Acos(\alpha)+Bcos(\beta)}\right]), \end{aligned} \tag{5.1}$$

where $arctan\left[\frac{Asin(\alpha)+Bsin(\beta)}{Acos(\alpha)+Bcos(\beta)}\right]$ is the phase of the signal. If we then take two signals:

$$\begin{aligned} S_1 &= Asin(\omega t+\alpha)+Bsin(\omega t+\beta), \\ S_2 &= Csin(\omega t+\alpha)+Dsin(\omega t+\beta). \end{aligned} \tag{5.2}$$

We get a phase lag:

$$\Delta\phi = arctan\left[\frac{Csin(\alpha)+Dsin(\beta)}{Ccos(\alpha)+Dcos(\beta)}\right] - arctan\left[\frac{Asin(\alpha)+Bsin(\beta)}{Acos(\alpha)+Bcos(\beta)}\right]. \tag{5.3}$$

Then if we rewrite it a little and take $r = A/B$ and $s = C/D$ we get:

$$\Delta\phi = arctan\left[\frac{s\ sin(\alpha)+sin(\beta)}{s\ cos(\alpha)+cos(\beta)}\right] - arctan\left[\frac{r\ sin(\alpha)+sin(\beta)}{r\ cos(\alpha)+cos(\beta)}\right]. \tag{5.4}$$

It is clear that if we take $r = s$ the phase lag will be 0. Figure 5.3 shows $\Delta\phi$ as a function of s, where $r = 1$ and $\delta\phi = \frac{1}{2}\pi$. We can see that for $s = 1$ the phase lag equals zero as mentioned above. For small values of s the phase lag tends to $\frac{1}{2}\delta\phi$ while for large values of s it tends to $-\frac{1}{2}\delta\phi$.

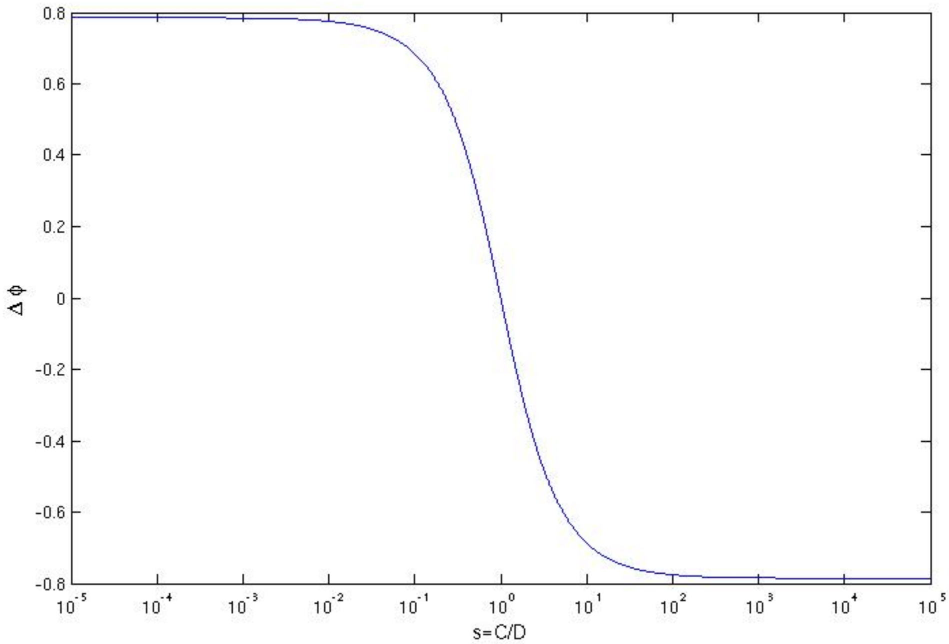

FIGURE 5.3: $\Delta\phi$ as a function of s for $r = 1$. The asymptotes at small and large s are $\frac{1}{2}\delta\phi$ and $-\frac{1}{2}\delta\phi$ respectively)

It is easy to see that these results are the same if we consider sums of sines as opposed to single sines, i.e. the following equation instead of equation 5.2:

$$
\begin{aligned}
S_1 &= A\ \Sigma_{i=1}^{N} sin(\omega t_i + \alpha_i) + B\ \Sigma_{i=1}^{N} sin(\omega t_i + \beta_i) \\
S_2 &= C\ \Sigma_{i=1}^{N} sin(\omega t_i + \alpha_i) + D\ \Sigma_{i=1}^{N} sin(\omega t_i + \beta_i)
\end{aligned}
\tag{5.5}
$$

5.2.2 Comparison with two-component model

The next step is to look at the two-component model in which the two signals consist of shots from a blackbody and a power-law component instead of two sine functions. I looked at the same cases as in the previous section, i.e. $r = s$ and a varying value of s for a fixed value of r. Looking at these cases it quickly became clear that the results where different than in the simple case of adding two sine functions. I learned that the relation between $\delta\phi$ and $\Delta\phi$ is not simple in this case but, not surprisingly, it depends on other parameters as well, such as z. This means that instead of deriving a relation between $\delta\phi$ and $\Delta\phi$, I had to take $\delta\phi$ as a free parameter in the simulation and see for which value the best fit to the observed phase lag is found. These simulations will be discussed in the next Chapter.

Chapter 6

Fitting the model to the data

In this Chapter I will describe my efforts to try and fit the simulations to the data for time lag as a function of energy (de Avellar et al. 2013) and rms as a function of energy (Berger et al. 1996). The first idea was to find the values for the parameters $\delta\phi$, kT, Γ and $z(= N_{BB}/N_{PL})$ to get the best fit to the time lag data keeping $A_{kT} = 0.03$ and $A_{\Gamma} = 0.03$, then take these four parameter values as fixed and find the values for A_{kT} and A_{Γ} to get the best fit to the rms data. This assumes that the values for the amplitudes have no effect on the time lag simulation, which is not exactly true but is a good first approximation. Eventually I also explore the case of fitting all the data (time lag and rms data) simultaneously.

6.1 Fitting the time-lag data

To fit the simulation to the time-lag data I set up a grid for the parameters $\delta\phi$, kT, Γ and $z(= N_{BB}/N_{\Gamma})$, then I simulate the time lags at the energy values used in the energy vs. time lag Figure in de Avellar et al. (2013) with respect to the reference energy of 4.2 keV. I then calculate a χ^2 (see below) for every combination of the parameter values in the grid and see which values give the smallest χ^2:

$$\chi^2 = \Sigma_{i=1}^{N} \frac{(S_i - O_i)^2}{\sigma_i^2}, \tag{6.1}$$

where S is the simulated data, O the observed data from de Avellar et al. (2013), and σ the errors on the observed data (also taken from de Avellar et al. 2013, the data points from their article are given in table 6.1). First I took a coarse grid with

E	Δt	σ
5.9870	-1.4285	2.601
8.0043	-11.3588	2.084
10.2155	-15.5400	2.680
12.7370	-27.5609	2.159
16.3060	-36.9686	4.615
18.9051	-50.5574	6.551

TABLE 6.1: Data points with error from de Avellar et al. (2013) used to fit the time-lag data.

parameter values as shown in table 6.2.

Parameter	Values
$\delta\phi$ (rad)	-0.1π, -0.3π, -0.5π, -0.7π, -0.9π
$< kT >$ (keV)	0.2, 0.5, 1, 1.5, 2, 3, 4, 5
$< \Gamma >$	1, 1.5, 2, 2.5, 3, 3.5
z	0.02, 0.05, 0.1, 0.15, 0.2, 0.25, 0.3

TABLE 6.2: Parameter values for the grid used to fit our model to the data from de Avellar et al. (2013)

Every parameter takes only 5 to 8 values in this range. Ideally one would take a much finer grid, but computing time increases exponentially for every extra parameter value added. So what I did instead was to find the best values of the parameters for this grid and run a refined grid around those values. The best parameter values found where: $\delta\phi = -0.9\pi$ rad, $< kT >= 5$ keV, $< \Gamma >= 1.5$ and $z = 0.02$, which give a χ^2 of 35.8 for 2 degrees of freedom. I then ran a finer grid around those values, the parameter values for this finer grid are shown in table 6.3:

Parameter	Values
$\delta\phi$ (rad)	-0.8π, -0.85π, -0.9π, -0.95π, $-\pi$
$< kT >$ (keV)	3.5, 4, 4.5, 5, 5.5, 6, 6.5
$< \Gamma >$	1.1, 1.3, 1.5, 1.7, 1.9, 2.1, 2.3, 2.5
z	0.01, 0.02, 0.03, 0.04, 0.05, 0.06

TABLE 6.3: Parameter values for the refined grid used to fit our model to the data from de Avellar et al. (2013)

This refined grid gave as best values for the parameters: $\delta\phi = -0.85\pi$ rad, $< kT >= 6.5$ keV, $< \Gamma >= 1.1$ and $z = 0.01$ with a χ^2 of 17.7 for 2 degrees of freedom. One could continue this process on and on to get better and better values for χ^2. A χ^2 of 17.7 is still pretty high but this is in part due to the fact that we are trying to fit 6 data points with 4 parameters, so even refining the grid a lot more will probably not yield a much better value for χ^2. Figure 6.1 shows the simulated data for the best obtained parameter values (line) compared with the data (circles) from de Avellar et al. (2013). The fit is not good, but it does show the correct trend, except that it flattens at the highest energies, whereas the observed data appear to follow a more or less linear relation.

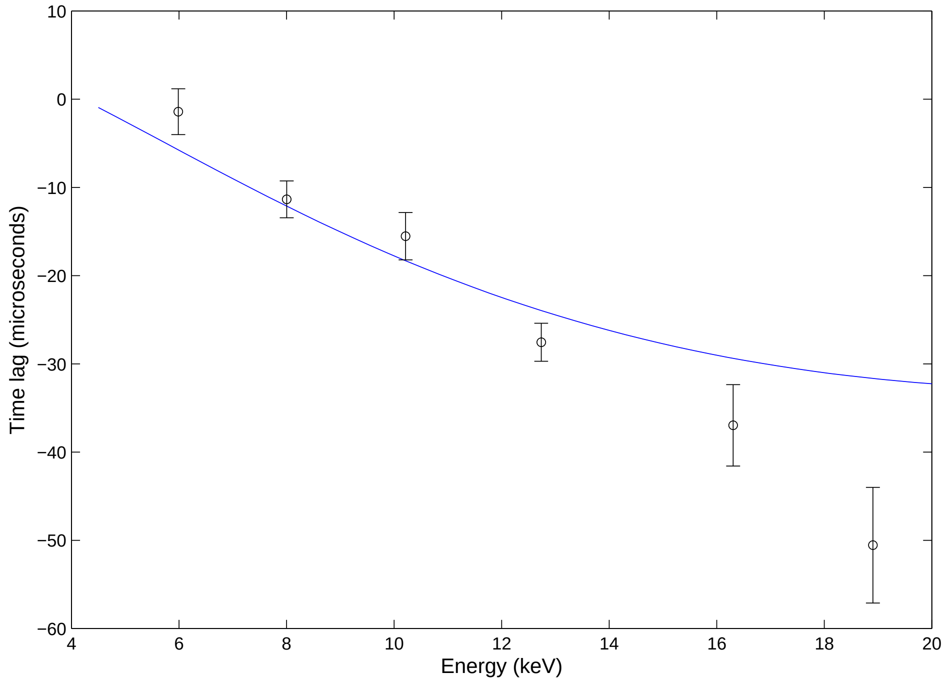

Figure 6.1: Showing the simulated data (line) for the best fitting parameters with the observed data (circles) from de Avellar et al. (2013).

6.2 Fitting the rms data

After finding the best values for the parameters $\delta\phi$, kT, Γ and z, the next step is to fit the rms data from Berger et al. (1996) by looking for the best values of A_{kT} and A_{Γ}. As noted before this assumes the time-lag data are not affected by changes in the amplitudes, which is not completely correct. Again I looked for the best χ^2 over a range of parameter values, this time using data points and errors from Berger et al. (1996, the data points from their article are given in table 6.4).

E	rms fraction	σ
5.0714	0.0489	0.0022
7.1428	0.0836	0.0028
9.4285	0.1222	0.0027
11.7857	0.1655	0.0039
14.7142	0.1777	0.0060
18.2142	0.1899	0.0157
22.2142	0.1824	0.0101
27.1428	0.1871	0.0312

TABLE 6.4: Data points with error from Berger et al. (1996) used to fit the rms data.

The range of parameters is this time between 0.01 and 0.18 with a stepsize of 0.01 for both amplitudes. The combination of values for the amplitudes which gives the best χ^2 is $A_{kT} = 0.18$ and $A_\Gamma = 0.09$ giving a χ^2 of 1002.5 for six degrees of freedom. This is a huge number for χ^2 meaning the fit is very bad as can be seen in Figure 6.2.

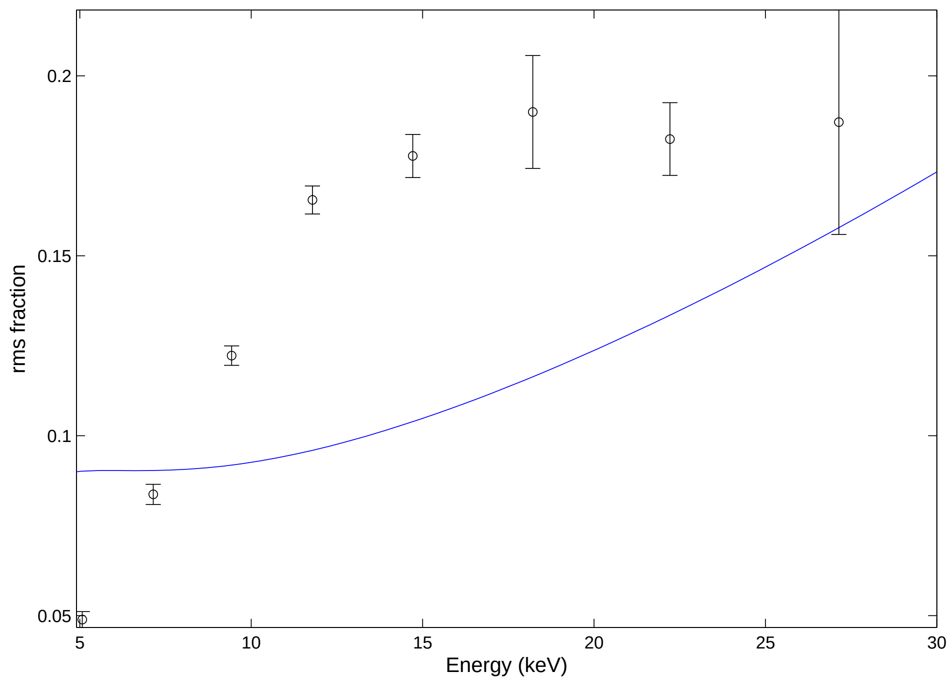

FIGURE 6.2: Showing the simulated data (line) for the best fitting parameters with the observed data (circles) from Berger et al. (1996).

It should be noted that the A_{kT} value found was also the largest that was tried in the simulation, meaning one might get a better fit for larger amplitudes. However the values of the amplitudes just scale the fitted line up or down, so while it is likely that a larger amplitude will result in a slightly better fit, it is clear that it will never result in a good fit. Because the problem is that the model fails to reproduce the shape of the data. It appears that this method of first fitting the time lag data with the parameters $\delta\phi$, kT, Γ and z and fixing those values to fit the rms data with the parameters A_{kT} and A_Γ does not result in a good fit. The obvious next step is trying to fit both data sets at the same time. In principle this is not much harder than fitting both separately, it does however increase the computing time by a large amount because that requires running one large grid with two extra dimensions instead of running two smaller grids one after the other.

6.3 Fitting time-lag and rms data simultaneously

For the case where we want to fit both sets of data for the time lags and the rms simultaneously we use a 6 dimensional grid with the parameters $\delta\phi$, kT, Γ, z, A_{kT} and A_Γ and find the best χ^2 for both fits combined. Because χ^2 is an additive quantity we can simply extend equation 6.1 to:

$$\chi^2 = \Sigma_{i=1}^{N_1} \frac{(S_{\Delta t,i} - O_{\Delta t,i})^2}{\sigma^2_{\Delta t,i}} + \Sigma_{j=1}^{N_2} \frac{(S_{rms,j} - O_{rms,j})^2}{\sigma^2_{rms,j}} \tag{6.2}$$

Where $S_{\Delta t}$ and S_{rms} are the simulated data for the time lags and rms respectively, $O_{\Delta t}$ and $\sigma_{\Delta t}$ are the observed data for the time lags and their errors respectively (from de Avellar et al. 2013) and O_{rms} and σ_{rms} are the observed data for the rms and their errors respectively (from Berger et al. 1996). The values of the parameters used for this simulation are shown in table 6.5

Parameter	Values
$\delta\phi$ (rad)	-0.1π, -0.3π, -0.5π, -0.7π, -0.9π
$< kT >$ (keV)	0.2, 0.5, 1, 2, 3, 4, 5
$< \Gamma >$	1, 1.5, 2, 2.5, 3, 3.5
z	0.02, 0.05, 0.1, 0.2, 0.3
A_{kT}	0.01, 0.05, 0.1, 0.2, 0.3
A_Γ	0.01, 0.05, 0.1, 0.2, 0.3

Table 6.5: Parameter values for the grid used to fit both the time-lag and rms data simultaneously

Again the grid is very coarse because the computing time increases exponentially when adding more parameter values to the grid. The parameter values that gave the best result were: $\delta\phi = -0.1\pi$ rad, $< kT >= 2$ keV, $< \Gamma >= 3$, $z = 0.1$, $A_{kT} = 0.05$ and $A_\Gamma = 0.2$, which give a χ^2 of 179.0 for 8 degrees of freedom. The resulting fits are shown in Figures 6.3 and 6.4. Figure 6.3 shows the best fit (line) for the time-lag data as well as the data points (circles) from de Avellar et al. (2013). We can see that the fit is formally not good. For lower energies the fit shows the correct trend of time lags decreasing with energy, but at higher energies the time lags increase again, which is the opposite to the observed data.

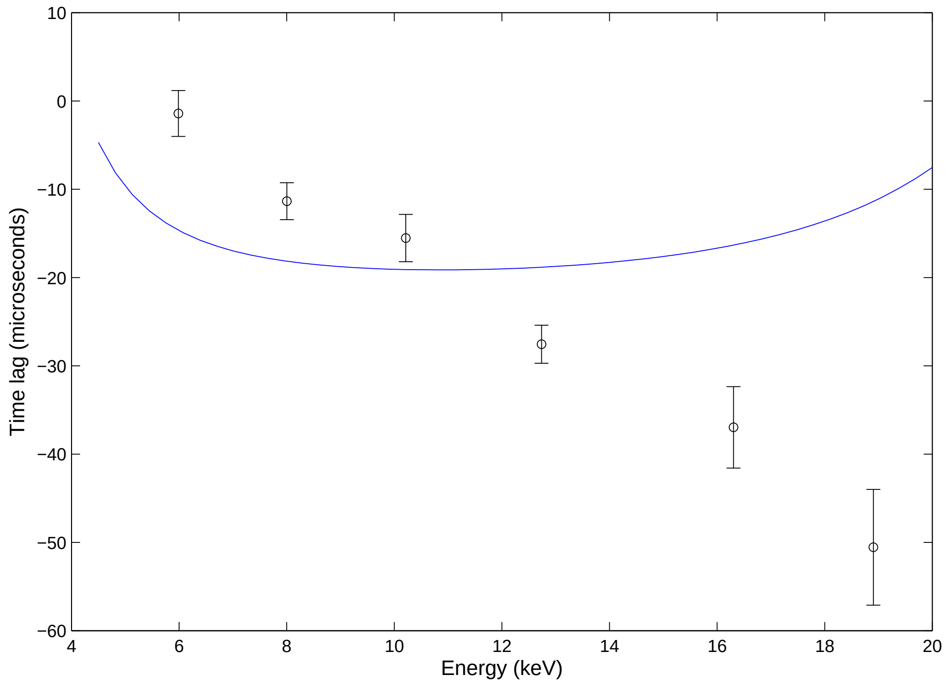

Figure 6.3: Fit that gives the best χ^2 when fitting both time-lag and rms data at the same time. Shown is the fit (line) as well as the observed data points (circles) from de Avellar et al. (2013).

Figure 6.4 shows the fit (line) to the rms data compared with the observed data (circles) from Berger et al. (1996). As we can see the fit follows the data points fairly well (except at around 25 keV), however, it seems unlikely that the trend shown is the correct one. The expectation is that the rms fraction flattens for higher energies instead of the dip shown by the model in Figure 6.4. In conclusion, both Figures show the correct trends at lower energies, but deviate from the observations at higher energies. To try and remedy this I introduced a high-energy cut off in the power law to the model, which will be described in the following section

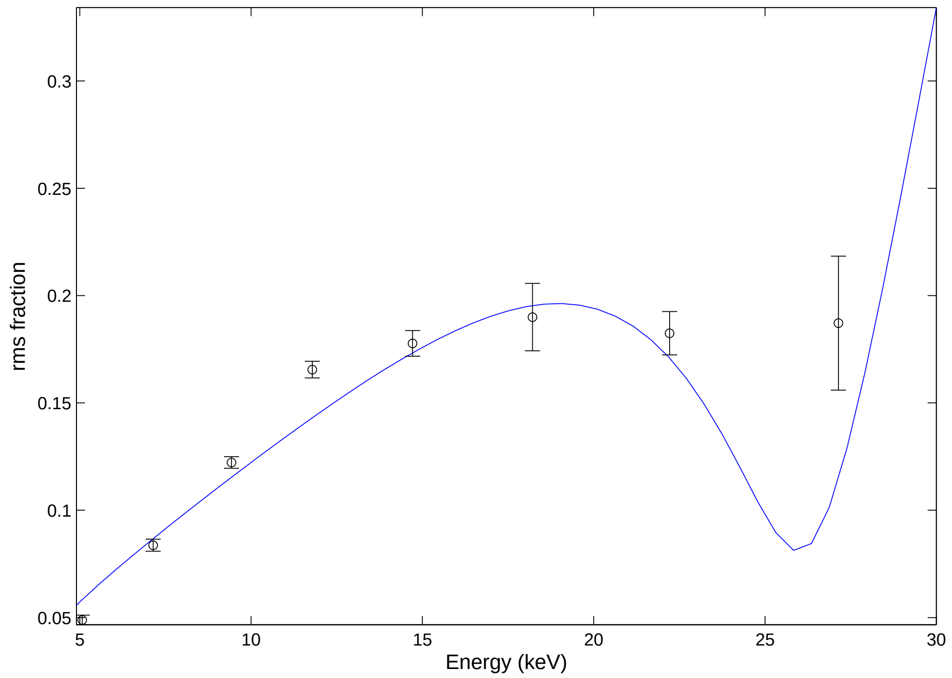

FIGURE 6.4: Fit that gives the best χ^2 when fitting both time-lag and rms data at the same time. Shown is the fit (line) as well as the observed data points (circles) from de Berger et al. (1996).

6.4 Model with a power law with a high-energy cut off

This section describes simulations done with a power law that has a high-energy cut off, as opposed to a simple power law used in the previous simulations. First I will justify the choice for a cut off, and then the fits from the resulting simulation will be shown.

6.4.1 Theory behind introducing a cut off

From the previous section we could see that the model fails to reproduce the data at high energies, so it seems logical to introduce a change that influences just the high energies. When looking at the blue (power law) and red (blackbody) lines in Figure 6.5 we can see that starting from the reference energy (green line) the flux density of the blackbody compared to that of the power law increases up to a certain energy and then decreases untill eventually the power law becomes the dominant component. This is similar to the trend shown in Figure 6.3, where initially the time lags increase up to a certain energy and then decrease again. If we look at a power law with a high-energy cut off (magenta) we can see that the relative contribution of the blackbody remains high at higher energies. This is of course dependent upon the value of the cut-off energy (E_c) as well as on the other parameters.

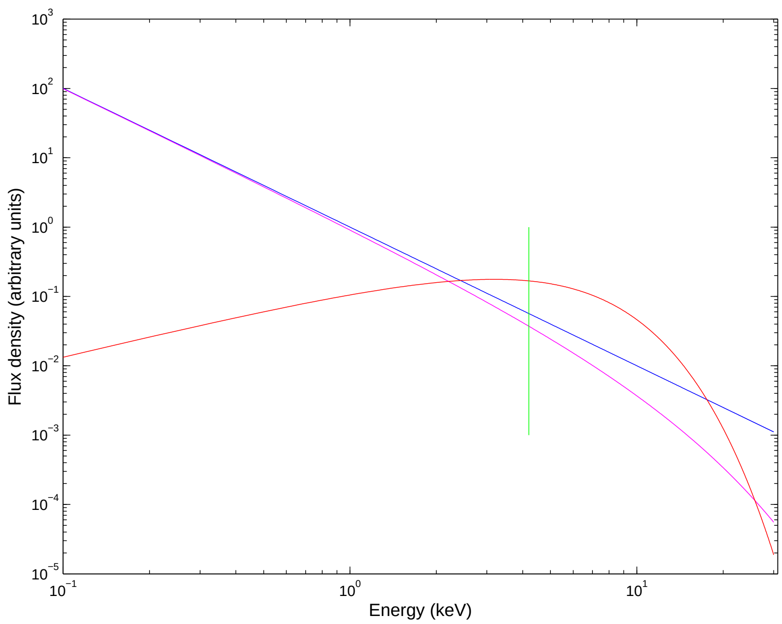

FIGURE 6.5: Used to illustrate why a power law with a cut off might improve the fits. The red line shows a blackbody, the blue line a power law without cut off, the magenta line a power law with a high-energy cut off, and the green line shows the reference energy (4.2 keV) used for the simulations. Parameter values used: $kT = 2$ keV, $\Gamma = 3$, $z = 0.02$ and $E_c = 10$ keV.

Introducing a cut off to the power law is not just some ad hoc change made to potentially improve the fit. The idea of a power law which has a cut off at a certain energy has been around for some time (White et al. 1985, Christian & Swank 1997). Aside from that, if we assume that the Comptonization in the corona is due to thermal electrons, which follow a Maxwell-Boltzmann distribution, a high-energy cut off comes out naturally. For a Maxwell-Boltzmann distribution there are fewer and fewer electrons as the energy increases. This means that there are also very few photons emited from the corona with an energy over a given E_c, resulting in a high-energy cut off in the power-law spectrum coming from the corona.

Before commiting to running a full simulation again, we should first verify that the introduction of a cut off will in fact improve the fits. If we look at Figure 6.6 we see that the model where the power law does not have a cut off (blue line) has time lags which strongly increase again at higher energies, while if we include a cut off at lower and lower energies (teal, E_c = 20 keV, yellow, E_c = 15 keV, green, E_c = 10 keV and red, E_c = 5 keV, lines) we see the increase becoming more shallow. For this case the cut off seems to alleviate some of the issues at higher energies, but not all of them as ideally we would have a more or less linear relation between time lag and energy as the data from de Avellar et al. (2013) seem to suggest.

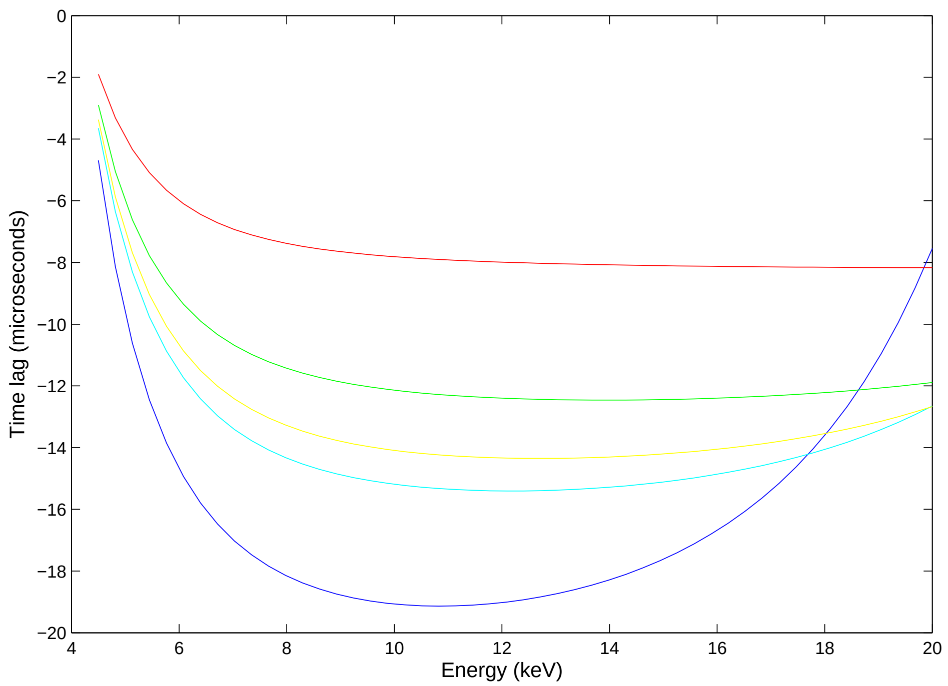

FIGURE 6.6: Showing time lags for one set of parameters with varying cut off energies. The blue line has no cut off, and it is the same fit as the one shown in Figure 6.3. The other lines show results using different values of the cut-off energy, E_c; 20 keV (teal line), 15 keV (yellow line), 10 keV (green line) and 5 keV (red line).

Figure 6.7 shows the influence of a cut off in the power law on the rms fits. We can see that in this case the introduction of a cut off just shifts the fit up and to the right, with the size of the shift depending on the value of E_c. We can see that using a high-energy cut off power law, as opposed to a power law without a cut off, will in this case probably not improve the fit by much.

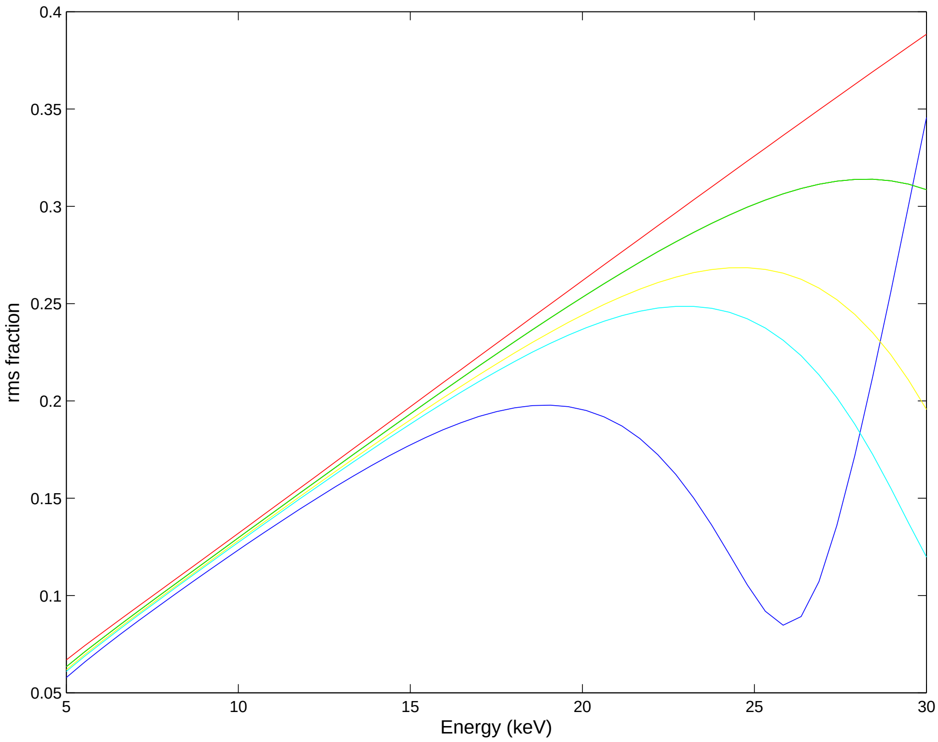

FIGURE 6.7: Showing rms fraction for one set of parameters with varying cut-off energies. The blue line has no cut off; it is the fit shown in Figure 6.4. The other lines show fits using different E_c; 20 keV (teal line), 15 keV (yellow line), 10 keV (green line) and 5 keV (red line).

Of course the addition of a cut-off energy might have different results for different sets of parameters. For example, if we look at Figure 6.8, which uses the parameters found for the first fit where I was just looking to fit the time lag separately ($\delta\phi = -0.85\pi$ rad, $< kT >= 6.5$ keV, $< \Gamma >= 1.1$, $z = 0.01$, $A_{kT} = 0.03$ and $A_\Gamma = 0.03$). The blue line shows the fit from Figure 6.1, whereas the red line shows a fit with the same parameters except that the power law has a cut off at $E_c = 10$ keV. We can see that in this case we can get a much better fit if we refine the parameters around the values given above. It should be noted, however, that these parameters gave a very bad fit to the rms data. So we can conclude that the introduction of a cut off energy for the power-law component will most likely improve the fits. The result of this new model will be shown in the next section.

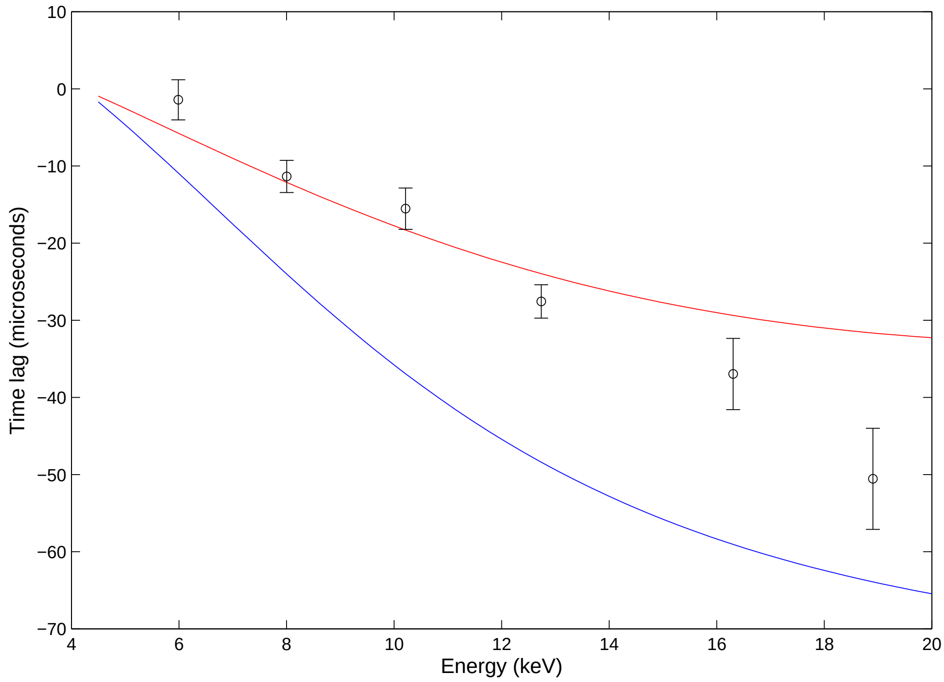

FIGURE 6.8: Showing the modelled time lags for the set of parameters from the first fit shown in Figure 6.1. The red line shows the fit from that Figure, i.e. using a power law without a cut off. The blue line shows the same model but with a cut off at E_c=10 keV.

6.4.2 Fits using a power law with a high-energy cut off

The model that has a power law with a cut-off energy introduces a new parameter E_c to be fitted, adding another dimension which increases the computing time by a lot. This is the reason there are only three possible values for E_c included in this simulation as well as a reduced number of values for some of the other parameters. Table 6.6 shows the parameter values used for this simulation.

Parameter	Values
$\delta\phi$ (rad)	-0.1π, -0.3π, -0.5π, -0.7π, -0.9π
$< kT >$ (keV)	0.2, 0.5, 1, 2, 3, 4, 5
$< \Gamma >$	1, 1.5, 2, 2.5, 3
z	0.02, 0.05, 0.1, 0.2, 0.3
A_{kT}	0.01, 0.05, 0.1, 0.2, 0.3
A_{Γ}	0.01, 0.05, 0.1, 0.2, 0.3
E_c	10, 15, 20

TABLE 6.6: Parameter values for the grid used to fit both the time lag and rms data simultaneously while also introducing a power law cut off at energy E_c

For this grid the values that give the lowest χ^2 are: $\delta\phi = -0.3\pi$, $kT = 3$ keV, $\Gamma = 1$, $z = 0.02$, $A_{kT} = 0.2$, $A_\Gamma = 0.01$ and $E_c = 15$. These values give χ^2 of 136.7 for eight degrees of freedom, about a 25% improvement over the model without a power law cut off. While this is a significant improvement, the χ^2 is still high. By refining the grid it can be brought lower, but the fits will most likely never become acceptable for this particular model. To get a better χ^2 value one would have to refine the model itself. The fits that give the best χ^2 value are shown in Figures 6.9 and 6.10 for the time lags and the rms fraction, respectively. In Figure 6.9 we can see an improvement at high energies over Figure 6.3, however the modelled time lags are still increasing at high energy whereas the observed time lags do not increase at those energies. The introduction of a cut off in the power-law component has improved the fit but clearly has not completely resolved the issue of the increasing time lags at higher energies.

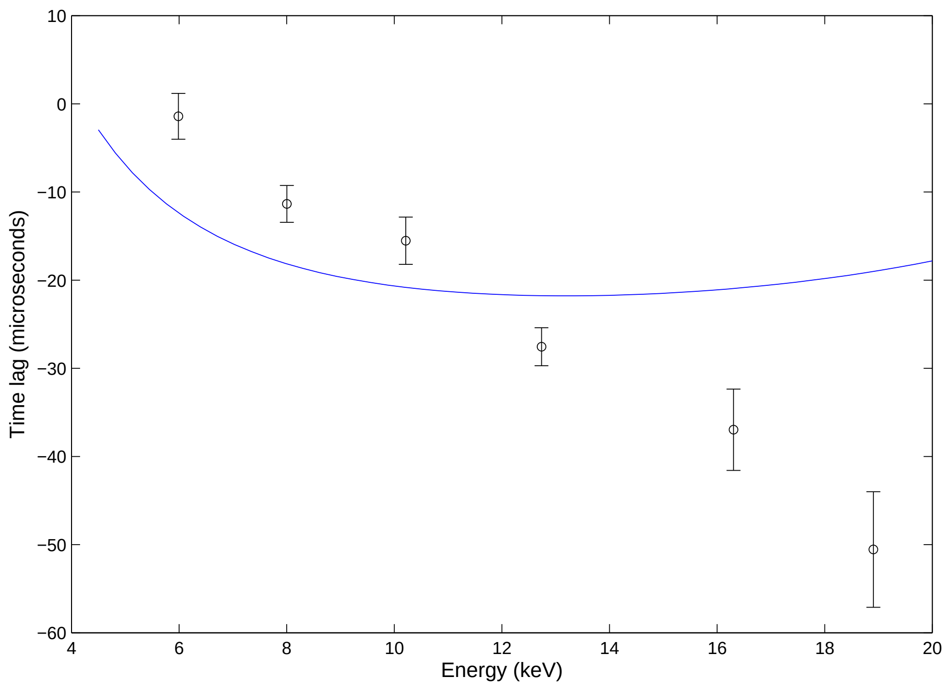

FIGURE 6.9: Showing the best fit for the time lags when trying to fit both the time lags and rms at the same time using a model with a power-law component with a cut off. Shown are the fit (line) and the observed data (circles) from de Avellar et al. (2013).

Finally Figure 6.10 also shows a slight improvement over Figure 6.4. However at high energies the rms fraction drops for the model used here while the observed rms remains more or less constant at high energies. We can see that the fits have improved when using a power law with high-energy cut off instead of a power law that has no cut off; however the fits still do not follow the relations shown by the observations. To improve the results further one would need to refine/complicate the model further, which is beyond the scope of this project. However, in the final Chapter I give some suggestions for possible improvements to be made to the model presented here.

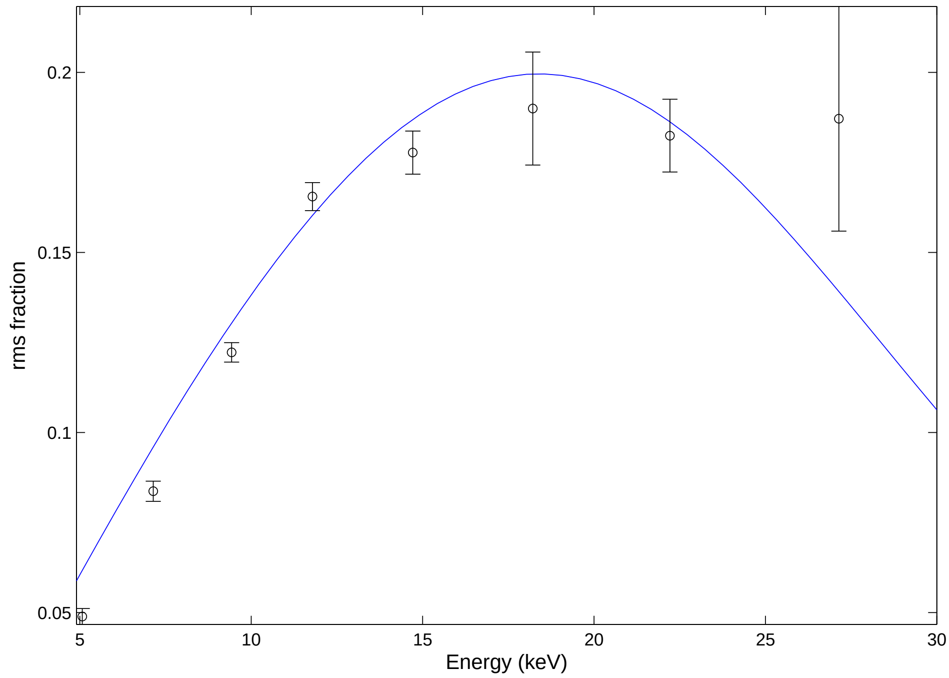

FIGURE 6.10: Showing the best fit for the rms fraction when trying to fit both the time lags and rms at the same time using a model with a power-law component with a cut off. Shown are the fit (line) and the observed data (circles) from Berger et al. (1996).

Chapter 7

Conclusion & outlook

7.1 Conclusion

The previous Chapter described the simulations ran for the two-component model used in this thesis and how it compares to the observational data from the lower kHz QPO of 4U 1636−53. The best values found for the final simulation with a cut off in the power law component were: $\delta\phi = -0.3\pi$ rad, $< kT >= 3$ keV, $< \Gamma >= 1$, $z = 0.02$, $A_{kT} = 0.2$, $A_\Gamma = 0.01$ and $E_c = 15$ keV. We saw that these values gave a qualitative good fit (i.e. showing the correct trends), but not a good quantitative fit, mostly for the time-lag plots. This is due to the fact that the two-component model used here is a gross oversimplification of the physical processes we think are present in LMXB sources, but even then the correct trends are observed. The fits can definitely be improved upon if the model would be further refined (see also next section).
Due to the way the code for this model is written, the definition for positive or negative phase lags is the opposite as that defined in de Avellar et. al. (2013), i.e. what they call positive lag shows up in this model as negative lag. However it is simply a matter of switching the sign of the input phase lag, $\delta\phi$, for the model to get to the definition used by them. This does not change anything except for the photons of which component would reach our hypothetical detector first. This leaves us with an input phase lag $\delta\phi = 0.3\pi$. This means the photons from the power-law component would reach our detector first. Physically one could interpret this as a situation where the blackbody photons coming directly from the neutron star are too weak to be detected, but they can gain energy due to Comptonization in the corona or due to reflection of the photons off the accretion disk. This is of course again a simplified view as the reflection spectra is unlikely to be a simple blackbody (see for example Sanna et. al. 2013 for a discussion on reflection in the source 4U 1636−53).

Main conclusion: The phase lag between the two components gives us a rough estimate on the distance between the sources of these components. At 800 Hz, a phase lag of 0.3π rad gives a time lag of 1.875×10^{-4} seconds (equation 2.2), which gives a distance $d = c\Delta t \approx 56$ km as a rough estimate between the blackbody and power-law component, i.e. a rough estimate on the size of the system. This number compares well with other results in the literature; e.g. Lee, Misra & Taam (2001), who found a size of 4 to 15 km for their much more sophisticated model.

In summary, the two-component model presented here gives a qualitative but not quantitative good fit to the observed data, as well as a reasonable size for the neutron-star + corona system given the simplicity of the model. To improve the results of the simulations the model would have to be extended/refined in some way.

7.2 Outlook

In this section I will shortly discuss some possible options for future work, either by extending the model presented here or by using a more mathematical approach using the Kompaneet's equation.

The first extension of the model that comes to mind is adding a third component, for example taking a blackbody component as the emission of the neutron star, a power-law component as the Comptonization of photons in the corona, and another component to model the reflection spectrum of the accretion disk. The reflected photons could possibly also interact with the corona again, making for an even more complex model.

Alternatively one could look at refining the model without adding extra components, for example what happens when we look at a frequency that varies with time as observed in kHz QPOs instead of keeping it constant. I also took the normalization factors of the two components to be constant and only allowed the temperature of the blackody and the index of the power law to vary. However, the normalization factors might also show fluctuations, most likely in a way where the fluctuations in the normalization 'follow' the fluctuations in the other parameters, for example if the temperature of the blackbody component goes up the normalization also goes up. Lastly the phase lag between the blackbody and the power law could also fluctuate since not every scattering in the corona or reflection on the accretion disk happens at the same point, causing slight differences in the input phase lag. It should be noted that any of the options discussed above will cause an increase in computing time. Adding more parameters to the simulation increases the run time of the simulation by a lot as discussed in Chapter 6. Also, unless additional data are used we will eventually run into the problem where we are trying to fit 14 data points with an equal number of parameters.

The mathematically correct way of modelling the Comptonization would be to look at the evolution of the photon-density described by the Kompaneets equation (e.g. Lee & Miller, 1998 and Lee, Misra & Taam, 2001). One could then see how variations in the input parameters would change the photon-density (Lee, Misra & Taam, 2001). This is however a significantly more complex problem.

7.3 Acknowledgements

I would like to thank everyone who helped me realize this master thesis. Firstly I would like to sincerely thank my supervisor Mariano Méndez for the many hours in which we discussed the research done for this thesis as well as always helping me with advise when I needed it.
Next I would like to thank my family and friends, especially Mom and Bennie, for their support in many ways during my study years. Without their support this thesis would not have been possible.
Finally I would like to thank all the students I shared the office with during these years, thank you for the good company and friendly work environment.

Bibliography

Barret, D., Olive, J. & Coleman Miller, M., 2006, MNRAS, 370, 1140

Bendat., J. & Piersol A., *Random data: Analysis and Measurement Procedures*, 1986, New York Wiley

Berger, M., et. al., 1996, ApJ, 469, 13

Caballero, I. & Wilms, J., 2012, MmSAI, 83, 230

Christian, D.J. & Swank, J.H., 1997, ApJS, 109, 177

de Avellar, M.G.B., Méndez, M., Sanna, A. & Horvath, J.E., 2013, MNRAS, 433, 3453

Dove, J.B., Wilms, J. & Begelman, M.C., 1997, ApJ, 487, 747

Frank, J., King, A. & Raine, D., *Accretion power in Astrophysics*, 2002, Cambride University Press

Kara, E., Fabian, A.C., Cackett, E.M., Miniutti, G. & Uttley, P, 2013a, MNRAS, 430, 1408

Kara, E., Fabian, A.C., Cackett, E.M., Steiner, J.F., Uttley, P., Wilkins, D.R & Zoghbi, A., 2013b, MNRAS, 428, 2795

Lee, H.C. & Miller, G.S., 1998, MNRAS, 299, 479

Lee, H.C., Misra, R. & Taam, R.E., 2001, ApJ, 549, 229

Méndez, M., van der Klis, M., Wijnands, R., Ford, E.C., van Paradijs, J. & Vaughan, B.A., 1998, ApJ, 505, L23

Pozdnyakov, L.A., Sobol, I.M. & Sunyaev R.A., 1983, ASPR, 2, 189

Pringle, J.E. & Rees, M.J., 1972, A&A, 21, 1

Sanna, A., *Accretion flow properties in low-mass X-ray binaries*, PhD Thesis, Rijksuniversiteit Groningen, Groningen, 2013

Sanna, A., Hiemstra, B., Méndez, M., Altamirano, D., Belloni, T. & Linares, M., 2013, MNRAS, 432, 1144

Shakura, N.I. & Sunyaev, R.A., 1973, A&A, 24, 337

Sobczak, G.J, McClintock, J.E., Remillard, R.A., Bailyn, C.D. & Orosz, J.A., 1999, ApJ, 520, 776

Stella, L. & Vietri, M., 1998, PRL, 82, 17

Thorne, K.S. & Price, R.H., 1975, ApJ, 195, L101

Uttley, P., M^cHardy, I.M., Vaughan, S., 2005, MNRAS, 359, 345

van der Klis, M., *Rapid X-ray Variability*, 2004, ed. Lewin, W.H.G. & van der Klis, M., 39-112

van der Klis, M., 1989, Annu. Rev. A&A, 27, 517

Vaughan, B.A. & Nowak, M.A., 1997, ApJ, 474, 43

White, N.E, Peacock, A & Taylor, B.G., 1985, ApJ, 296, 475